TU Delft

Delft University of Technology

Document Version
Final published version

Licence
Dutch Copyright Act (Article 25fa)

Citation (APA)
Xiao, Y., Wang, Z., Jin, P., Zhuang, H., Zhao, W., Tan, J., & Zhou, B. (2026). Multi-objective optimization and performance analysis of a 10 MW offshore wind-wave hybrid system with built-in wave energy converters. *Ocean Engineering*, *358*, Article 125815. https://doi.org/10.1016/j.oceaneng.2026.125815

Important note
To cite this publication, please use the final published version (if applicable).
Please check the document version above.

Copyright
In case the licence states “Dutch Copyright Act (Article 25fa)”, this publication was made available Green Open Access via the TU Delft Institutional Repository pursuant to Dutch Copyright Act (Article 25fa, the Taverne amendment). This provision does not affect copyright ownership.
Unless copyright is transferred by contract or statute, it remains with the copyright holder.

Sharing and reuse
Other than for strictly personal use, it is not permitted to download, forward or distribute the text or part of it, without the consent of the author(s) and/or copyright holder(s), unless the work is under an open content license such as Creative Commons.

Takedown policy
Please contact us and provide details if you believe this document breaches copyrights.
We will remove access to the work immediately and investigate your claim.

This work is downloaded from Delft University of Technology.

Ocean Engineering 358 (2026) 125815

Contents lists available at ScienceDirect

Ocean Engineering

journal homepage: www.elsevier.com/locate/oceaneng

Research paper

Multi-objective optimization and performance analysis of a 10 MW offshore wind-wave hybrid system with built-in wave energy converters

Yi Xiao [a,b], Zedong Wang [a,b], Peng Jin [b], Hongkun Zhuang [c], Wenhua Zhao [d], Jian Tan [e], Binzhen Zhou [a,b,f,*]

[a] State Key Laboratory of Subtropical Building and Urban Science, South China University of Technology, Guangzhou, 510641, China
[b] School of Civil Engineering and Transportation, South China University of Technology, Guangzhou, 510641, China
[c] School of Marine Science and Engineering, South China University of Technology, Guangzhou, 511400, China
[d] School of Civil Engineering, The University of Queensland, Brisbane, 4072, Australia
[e] Faculty of Civil Engineering and Geosciences, Delft University of Technology, Delft, 2628 CD, Netherlands
[f] China Ship Scientific Research Center, Wuxi, 214082, China

ARTICLE INFO

Keywords:
Multi-objective optimization
Hybrid energy system
Offshore wind
Wave energy converter
PTO system

ABSTRACT

Integrating wave energy converters (WECs) into floating offshore wind turbines (FOWTs) offers the potential to reduce both power generation costs and platform motions. Placing WECs within the hollow side columns of the wind turbine platform represents a novel approach, providing protection against direct wave impact and corrosion. However, the mechanisms and performances of such hybrid systems remain unclear. In this study, a novel wind-wave hybrid system is proposed and investigated, consisting of a 10 MW OO-STAR type platform with built-in WECs. A frequency-domain model based on potential flow theory is developed, and a multi-objective optimization framework using the NSGA-II algorithm is applied to optimize the power take-off (PTO) parameters. Results indicate that global optimization across operational sea-state ranges can effectively mitigates abnormally large pitch motions in specific period ranges, thereby reducing the maximum pitch response across all sea states and broadening the energy absorption bandwidth. By introducing the metric of annual average power generation per unit mass, the economic efficiency of the system is further enhanced. Moreover, the mechanisms by which the PTO parameters influence motion responses and power generation performance of the hybrid system are revealed. These findings provide practical guidance for design and application of wind-wave hybrid systems.

1. Introduction

Global energy demand has been steadily increasing over the past few years (Farghali et al., 2023) (Wang and Azam, 2024). The continued reliance on conventional fossil fuels leads to severe environmental pollution (Abbasi et al., 2022). In response, the pursuit of net-zero emissions by 2050 has accelerated the global transition toward clean and renewable energy sources (Deutch, 2020). Among the various renewable energy options, ocean renewable energy has attracted increasing attention (Taveira-Pinto et al., 2020).

Offshore wind energy is currently one of the most mature and commercially established forms of ocean renewable energy (Beirão and Mendes, 2025). Depending on the platform configuration, FOWTs are generally classified into four main types: spar, barge, tension-leg, and semi-submersible platforms (Jansen et al., 2020). Among these, semi-submersible platforms have been most widely adopted owing to their advantages in construction feasibility, transportation efficiency, and adaptability to a wide range of water depths (Yin et al., 2024). Representative semi-submersible wind turbine designs include the 2 MW WindFloat WF1 (Roddier et al., 2010), 5MW OC4 DeepCwind (Robertson, 2014), 8.4 MW WindFloat Atlantic (Duarte et al., 2022), 10 MW OO-STAR (Yu et al., 2018) (Wang et al., 2025a), 15 MW UMaine VolturnUS-S (Allen et al., 2020), and 22 MW IEA Wind concepts (Zahle et al., 2024) (Wang et al., 2025b). An evident trend toward increasing installed capacity can be observed (Soares-Ramos et al., 2020). However, large-capacity wind turbines are still predominantly at the conceptual design stage or limited to scaled model testing. Wave energy represents another promising form of ocean renewable energy (Mwasilu and Jung, 2019). Based on energy conversion principles, WECs can be generally categorized into three types: overtopping, oscillating water

* Corresponding author. State Key Laboratory of Subtropical Building and Urban Science, South China University of Technology, Guangzhou, 510641, China.
E-mail address: zhoubinzhen@scut.edu.cn (B. Zhou).

https://doi.org/10.1016/j.oceaneng.2026.125815
Received 12 March 2026; Received in revised form 18 April 2026; Accepted 27 April 2026
Available online 4 May 2026
0029-8018/© 2026 Elsevier Ltd. All rights are reserved, including those for text and data mining, AI training, and similar technologies.

column, and oscillating body types (Zhou et al., 2024). Oscillating body WECs are further classified into heaving-type and flap-type configurations, and have been extensively investigated due to their flexible deployment and ease of integration with coastal and offshore structures (Zheng et al., 2025) (Huang et al., 2025a). Despite these advantages, the independent development of offshore wind and wave energy technologies remains constrained by strong intermittency, high standalone costs, and challenges related to structural stability, which collectively hinder large-scale deployment (Rehman et al., 2023) (Johnston et al., 2020).

To address these challenges, various concepts of wind-wave hybrid systems have been proposed. In such systems, WECs are installed on FOWT platforms, allowing the sharing of mooring systems, electrical cables, and other infrastructure. This integration not only supplements the energy output of FOWTs but also contributes to a reduction in the levelized cost of energy (LCOE) (Lin et al., 2025) (Ferrari et al., 2020). With appropriate parameter selection and layout design, WECs can further suppress the motion responses of FOWTs and enhance overall system stability (Zhu et al., 2024) (Li et al., 2023). Representative concepts include STC (Muliawan et al., 2013), SFC (Michailides et al., 2014), WindFloat-HWEC (Hu et al., 2020), and DeepCwind-WaveStar (Jin et al., 2023a), most of which integrate semi-submersible FOWT with oscillating bodies. Building upon these general concepts, Xiao et al. (2025) proposed a novel wind-wave hybrid system featuring built-in WECs installed within the hollow side columns of a 5 MW OC4 DeepCwind platform, providing additional benefits such as protection against seawater-induced corrosion and wave impacts. Extending this built-in WEC concept, the present study applies the design to a 10 MW OO-STAR type semi-submersible floating wind turbine.

Following the development of these hybrid system concepts, substantial research efforts have been devoted to analyzing their motion responses and power performance, as well as optimizing key system parameters. Zhou et al. (2023a) employed a single-objective numerical optimization approach to determine the optimal PTO damping that maximizes wave power generation under different conditions, based on which the optimal WEC shape and layout were further identified under the same objective. Da Silva et al. (2022) applied a multi-objective optimization algorithm to tune PTO stiffness and damping, aiming to maximize wave power absorption while minimizing nacelle horizontal acceleration. Huang et al. (2024) combined surrogate modeling with the NSGA-II algorithm to optimize six parameters of a hydraulic PTO system, achieving simultaneous maximization of wave power generation and minimization of pitch motion. In another study, Huang et al. (2025b) employed the NSGA-II algorithm to optimize WEC geometry, targeting maximum power generation a together with minimum pitch and heave responses of the hybrid system. As a result, wave power generation was increased by 292.68%, while heave and pitch motions were reduced by 36.96% and 73.65%, respectively. Furthermore, Neshat et al. (2024) proposed the multi-objective swarm optimization method (DMOGWA) for WEC design and PTO parameters, leading to a 138.5% increase in average power generation and a 41% reduction in nacelle acceleration. Overall, multi-objective optimization approaches have been increasingly adopted for wind-wave hybrid systems, with most studies focusing on maximizing energy generation while minimizing platform or nacelle motion responses.

However, existing studies on the optimization of wind-wave hybrid systems exhibit two major limitations. First, optimization is often conducted based on a single representative sea state, while the implications of such point-based optimization for system performance under varying sea conditions remain insufficiently explored. Second, although multi-objective optimization is widely adopted, it is primarily used to generate optimal solution sets, with limited attention devoted to examining how design variables evolve along the Pareto front and how these variations govern performance trade-offs. Consequently, the physical mechanisms underlying performance variations are not fully interpreted, which constrains the understanding of trade-off behavior and limits the practical application of Pareto-optimal solutions in engineering design. To address these issues, the present study makes the following novel contributions. First, a systematic comparison is conducted between point-based PTO optimization under a single representative sea state and global PTO optimization over operational sea-state ranges. The results demonstrate that the latter effectively avoids abnormal motion amplification in adjacent period ranges and yields more robust motion and power performance. Second, the optimization outcomes are further investigated through a detailed analysis along the Pareto front to elucidate how variations in PTO parameters shape the trade-off between motion reduction and power generation. Meanwhile, the underlying mechanism of pitch motion reduction induced by the built-in wave energy converters is further clarified.

The remainder of this paper is structured as follows. Section 2 outlines the configuration of the novel hybrid system. Section 3 details the methodology and model validation. Section 4 compares the results of different multi-objective optimization strategies. Section 5 examines the impact of PTO parameters on the system performance. Section 6 summarizes the key conclusions.

2. Hybrid system

2.1. Structural design and key parameters

The novel wind-wave hybrid system is based on an OO-STAR type semi-submersible floating wind turbine. A 10 MW wind turbine is installed on the top of the central column, while three heave oscillating body WECs (WEC#1, WEC#2, and WEC#3) are built into the three hollow side columns of the platform. The schematic configuration of the hybrid system is presented in Figs. 1 and 2, and the main parameters are listed in Table 1. Further details regarding the design of the wind turbine platform can be found in Ref. (Yu et al., 2018).

The wind turbine platform is designed to operate in deep-sea conditions with a depth of 130 m. The incident regular waves travel in the positive x-direction (Fig. 2), under which the hybrid system is allowed to move in six degrees of freedom. The built-in WECs can be simplified as vibration systems consisting of mass, stiffness, and damping, and are treated as non-hydrodynamic components in subsequent calculations. The mass block of each device is designed as a flat cylindrical body, with



Fig. 1. Structural design schematic of the hybrid system.

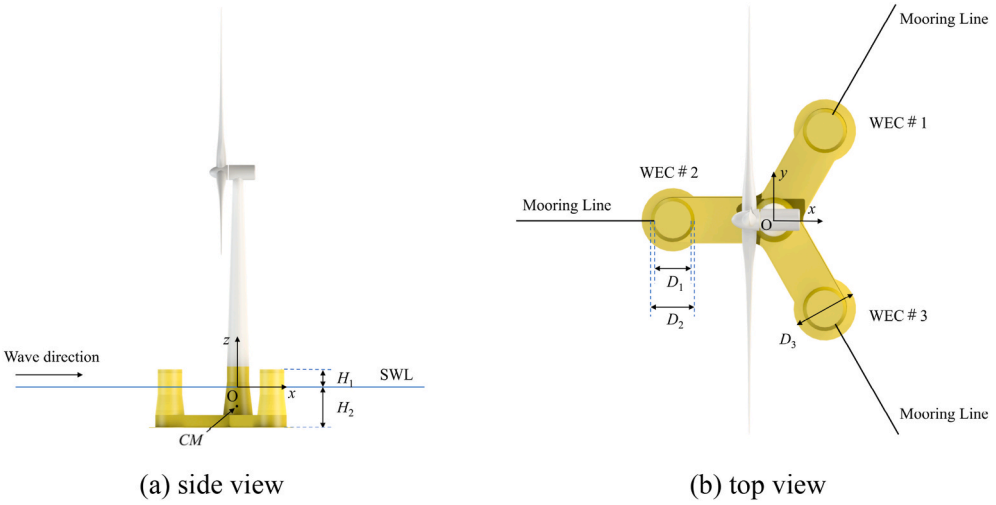

Fig. 2. Dimensional diagram of the hybrid system.

Table 1
Key parameters of the hybrid system.

Item	Symbol	Value and unit
Draft	H_1	22.00 m
Elevation of offset column above SWL	H_2	9.50 m
Diameter of offset (upper) columns	D_1	13.40 m
Diameter of base columns	D_2	15.80 m
Diameter of main column	D_3	22.80 m
Total platform mass	M	2.11×10^7 kg
Position of mass center below SWL	CM	15.85 m
Platform roll inertia about CM	I_{xx}	9.13×10^9 kg·m^2
Platform pitch inertia about CM	I_{yy}	9.13×10^9 kg·m^2
Platform yaw inertia about CM	I_{zz}	1.63×10^{10} kg·m^2
Platform resonant period in surge direction	T_{surge}	209.44 s
Platform resonant period in heave direction	T_{heave}	20.27 s
Platform resonant period in pitch direction	T_{pitch}	16.53 s
Hydrostatic restoring coefficient in heave direction	C_{33}	5.51×10^6 N/m
Radiation damping in heave direction at resonance	$\lambda_{rad,33}$	1.15×10^4 N· s/m

its center of gravity located at the middle of the platform side column (6 m below the still water level). This layout is to achieve a larger motion stroke for enhancing the power generation, while simultaneously improving the stability of the hybrid system.

The WECs are connected to the platform through vertical linear PTO systems, which satisfy the linear constraint assumption by allowing only relative heave motion with the platform. Power generation is achieved through this relative heave motion. In this system, the mass, stiffness, and damping not only directly influence their motion response but also play a significant role in the power performance of the hybrid system. Therefore, these parameters are selected as key input variables for detailed analysis in the subsequent optimization.

To simplify the parameters and enhance the generality of the optimization analysis, the three PTO parameters are nondimensionalized (Chen et al., 2018). The dimensionless mass, stiffness, and damping are defined as follows:

$$\overline{m} = \frac{m}{M} \tag{1}$$

$$\overline{k} = \frac{K_{PTO}}{C_{33}} \tag{2}$$

$$\overline{b} = \frac{B_{PTO}}{\lambda_{vis,33} + \lambda_{rad,33}} \tag{3}$$

where m denotes the mass of a WEC, while K_{PTO} and B_{PTO} are the PTO stiffness and damping, respectively. $\lambda_{vis,33}$ denotes the hydrodynamic viscous damping at the resonant period of the FOWT mass.

Table 2
The value ranges of optimization parameters.

Item	Value range
$\overline{m}$	0.01-0.2
$\overline{k}$	0.01-1.0
$\overline{b}$	0.01-2.0

The lower bounds of all dimensionless parameters are set to values greater than zero, consistent with the passive PTO control assumption adopted in this study. The upper bound of the dimensionless mass is estimated based on the platform ballast mass, combined with the available space inside the side columns and the density of the mass block material (steel). The upper bounds of the dimensionless stiffness and damping are determined based on the chosen dimensionless mass, together with preliminary trial calculations. Finally, the parameter ranges are summarized in Table 2.

In terms of the maximum dimensionless mass, the maximum achievable relative heave peak of the WECs is estimated to be approximately 10 m, based on a steel density of 7850 kg/m^3. This value is adopted as a constraint on the relative heave motion between the platform and the WECs in the subsequent optimization, to ensure structural safety and design feasibility.

2.2. Mooring configuration

The hybrid system is moored using a three-cable catenary mooring system, with the cables uniformly distributed at 120° intervals (Fig. 3). One end of each cable is anchored to the seabed, while the other end is attached to the side columns of the platform, as illustrated in Fig. 3b. Different from Ref. (Yu et al., 2018), the clump mass is neglected to facilitate optimization in the frequency-domain calculation model, whereas other parameters remain unchanged. The detailed parameters are listed in Table 3.

The open-source mooring system modeling tool MAP++ (Mooring Analysis Program) (Masciola et al., 2014), developed by the National Renewable Energy Laboratory (NREL), is employed. This program is mainly used for modeling mooring systems of offshore structures such as floating wind turbines, and is particularly suited for integration with platforms like OpenFAST. By using MAP++, the mooring system can be transformed into an equivalent stiffness matrix and incorporated into the multi-body motion equations in the frequency-domain analysis. The resulting numerical values are presented in Table 4.

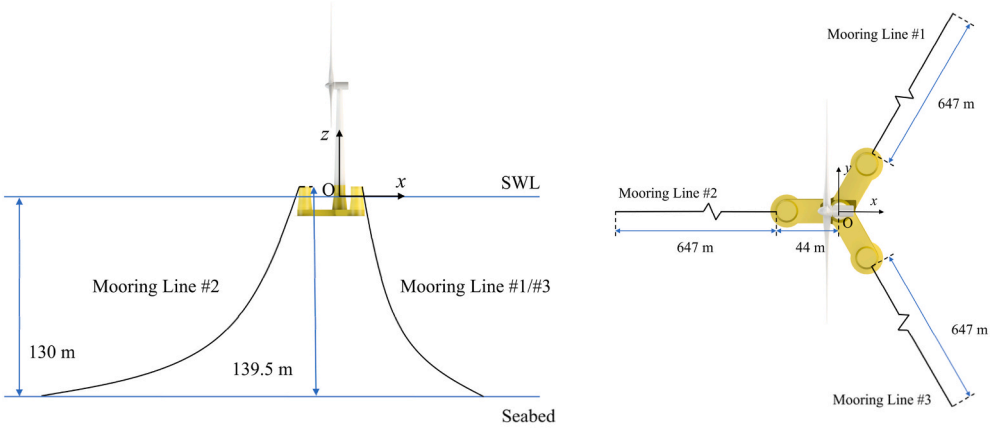

(a) side view (b) top view

Fig. 3. Dimensional diagram of the mooring system.

Table 3
Key parameters of the mooring system.

Item	Unit	Value
Number of lines	-	3
Angle between adjacent lines	deg	120
Unstretched mooring line length	m	703.00
Vertical position of fairleads above MSL	m	9.5
Anchor position below MSL	m	130
Radius to anchors from platform centerline	m	691
Radius to fairleads from platform centerline	m	44
Equivalent mass per length in air	kg/m	375.38
Extensional stiffness EA	N	1.506×10^9
Hydrodynamic added mass coefficient	-	0.8
Hydrodynamic drag coefficient	-	2.0
Effective hydraulic diameter of the chain	m	0.246

2.3. Environmental conditions

The sea-state data used in this study are provided by the National Ocean Technology Center (NOTC) of China, based on one-year measurements in a sea area of the South China Sea near Hainan Province. The measurement site is located at 19.34°N, 113.76°E, with a water depth ranging from approximately 100 to 200 m, which matches the design operational depth of the OO-STAR floating wind turbine platform. The joint probability distribution of wave height and wave period in this region is shown in Fig. 4. It also illustrates the representative operational sea states corresponding to different cumulative probability levels, the detailed definitions of which are provided in Section 4.1.2. This data set will be used in the subsequent assessment of the hybrid system's motion responses and power generation performance.

3. Method

3.1. Numerical model

A frequency-domain wave-structure interaction calculation method has been developed for the hybrid system, in which the hydrodynamic coefficients are obtained for the platform alone using a higher-order boundary element method (Teng and Taylor, 1995). This method enables rapid assessment of the motions of the platform and the built-in WECs, thereby supporting subsequent performance analysis and parameter optimization. This method is established under several assumptions based on the linear potential flow theory, in which the fluid is considered incompressible, inviscid, and flow is irrotational, and the wave amplitude is assumed to be small. Under the action of incident waves with angular frequency ω, the motion equation for the i-th ($i = 1, \ldots,18$) mode of the WECs, which are non-hydrodynamic structures, considering the constraints of the PTO, is given as:

$$\sum_{j=1}^{24}\left[-\omega^2 m_{ij} - \mathrm{i}\omega b_{\mathrm{PTO},ij} - k_{\mathrm{PTO},ij}\right] x_j = \delta_{\mathrm{L},i} f_{\mathrm{L},i} \tag{4}$$

And the motion equation for the i-th ($i = 19, \ldots,24$) mode of the platform is:

$$\sum_{j=1}^{24}\left[-\omega^2\left(m_{ij}+\mu_{ij}\right) - \mathrm{i}\omega\left(\lambda_{ij}+\lambda_{\mathrm{vis},ij}+b_{\mathrm{PTO},ij}\right) + C_{ij} + k_{\mathrm{stiff},ij} - k_{\mathrm{PTO},ij}\right] x_j$$
$$= f_{\mathrm{ex},i} - \sum_{n=1}^{3}\delta_{\mathrm{L},6n+i-24} f_{\mathrm{L},6n+i-24} \tag{5}$$

where m_{ij}, μ_{ij}, λ_{ij}, $\lambda_{\mathrm{vis},ij}$ and C_{ij} denote the mass, added mass, radiation damping, hydrodynamic viscous damping, and hydrostatic restoring coefficient associated with the motion in mode i induced by motion in mode j, respectively. $b_{\mathrm{PTO},ij}$ and $k_{\mathrm{PTO},ij}$ represent the ij-th element of the internal PTO damping matrix B_{PTO} and stiffness matrix K_{PTO}. $k_{\mathrm{stiff},ij}$ corresponds to the ij-th element of the mooring stiffness matrix K_{stiff}. x_j, $f_{\mathrm{ex},i}$, and $f_{\mathrm{L},i}$ represent the wave-induced complex displacement response, wave excitation force, and constraint force, respectively. The indicator $\delta_{\mathrm{L},i}$ is defined as:

$$\begin{cases} \delta_{\mathrm{L},i} = 0 & i = 6n-3, n = 1,2,3 \\ \delta_{\mathrm{L},i} = 1 & i \neq 6n-3, n = 1,2,3 \end{cases} \tag{6}$$

Table 4
Equivalent mooring stiffness matrix (unit: kg·s^{-2}\kg·m·s^{-2}\kg·m·s^{-2}·rad^{-1}\kg·m^2·s^{-2}·rad^{-1}).

Direction	Surge	Sway	Heave	Roll	Pitch	Yaw
Surge	3.34×10^4	0.00×10^0	-2.00×10^2	0.00×10^0	1.12×10^6	0.00×10^0
Sway	1.00×10^2	3.34×10^4	0.00×10^0	-1.12×10^6	4.70×10^1	4.80×10^1
Heave	-2.00×10^2	1.00×10^2	3.16×10^4	-4.60×10^1	-6.80×10^1	0.00×10^0
Roll	-5.00×10^2	-1.11×10^6	1.90×10^1	5.80×10^7	-4.41×10^0	-4.50×10^1
Pitch	1.11×10^6	-1.00×10^1	-3.50×10^1	4.89×10^0	5.80×10^7	0.00×10^0
Yaw	1.30×10^1	4.80×10^1	-1.70×10^1	1.47×10^1	5.08×10^0	6.82×10^7

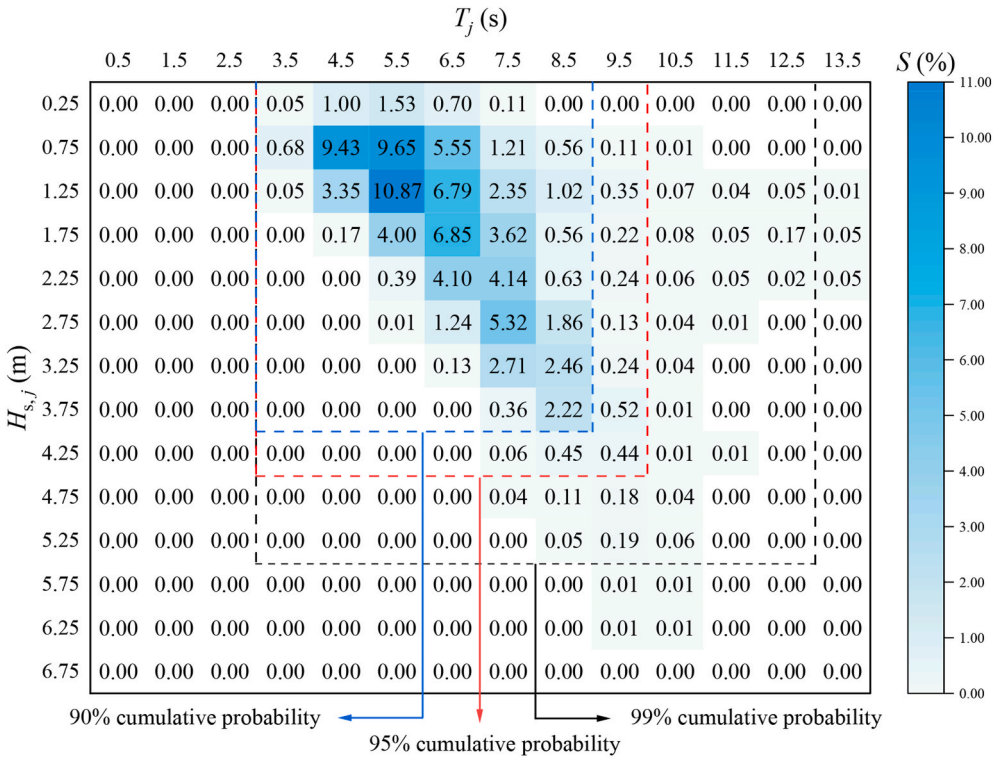

Fig. 4. Joint probability distribution of significant wave height and mean wave period in South China Sea.

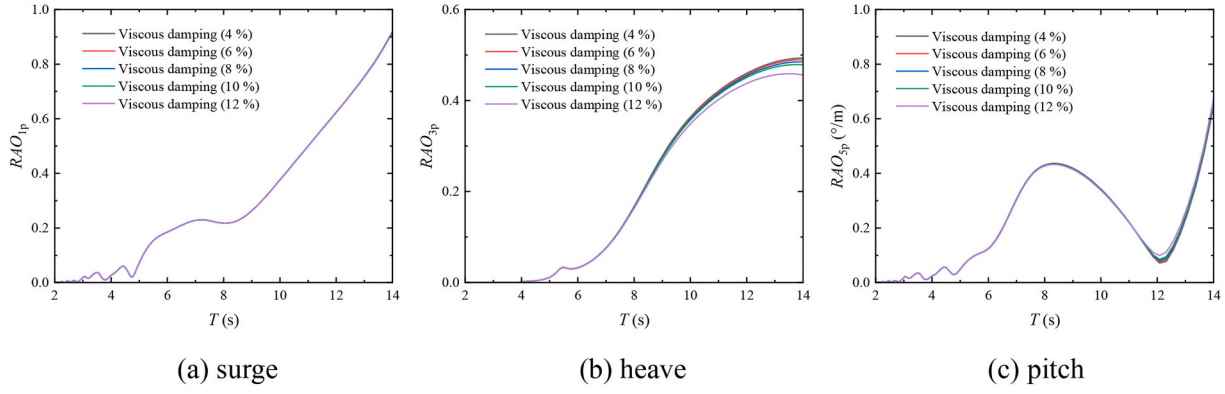

Fig. 5. Comparison of platform motions under different viscous damping.

Transformation matrices are used to transfer the constraint forces from their application points to the platform center of gravity. Further details on the constraint force treatment are provided in Refs. Zhou et al. (2023a,b).

The potential-flow-based calculation method neglects the effect of fluid viscosity, which can lead to significantly amplified motion responses of the hybrid system at resonant frequencies. To mitigate this effect, linear hydrodynamic viscous damping is added to the semi-submersible platform during the calculation. The viscous correction for the semi-submersible platform is usually calculated using the critical damping method, with a dimensionless damping ratio ζ of 8 %, which has been demonstrated to reasonably represent the viscous effects in previous studies (Zhou et al., 2023b) (Jin et al., 2023b). In addition, to examine the applicability of this value to the specific platform configuration considered in this study, a sensitivity analysis is conducted by comparing platform motions under different viscous damping in Fig. 5. The results indicate that the influence of damping variation on the motion responses within the considered sea-state range is limited, as the dominant wave periods are generally away from the resonance region. Based on the above references and the present analysis, the dimensionless damping ratio ζ of 8 % is adopted in this study.

The hydrodynamic viscous damping of the platform $\lambda_{\mathrm{vis},ij}$ can be computed using the following formula:

$$\lambda_{\mathrm{vis},ij} = 2 \cdot \zeta \cdot \sqrt{\left(m_{ij} + \mu_{ij}\right) \cdot \left(k_{\mathrm{stiff},ij} + C_{ij}\right)} \tag{7}$$

Finally, the hydrodynamic viscous damping in the surge, heave, and pitch directions is calculated in Table 5.

3.2. Wave power calculation

The power generation $P_k(T)$ of the k-th WEC in the hybrid system under a unit wave amplitude is:

$$P_k(T) = \frac{1}{2}\left(\frac{2\pi}{T}\right)^2 B_{\mathrm{PTO},k} \left|z_{r,k}\right|^2 \tag{8}$$

where T is the wave period of the incident waves, B_{PTO} is the PTO

Table 5
The hydrodynamic viscous damping of the DTU 10 MW platform.

Direction	Symbol	Value
Surge	$\lambda_{vis,11}$	1.79×10^5 N·s/m
Heave	$\lambda_{vis,33}$	2.81×10^6 N·s/m
Pitch	$\lambda_{vis,55}$	3.45×10^7 N·m·s/rad

damping, and z_r denotes the relative heave motion between the WEC and the platform under a unit wave amplitude.

The annual average power generation of each WEC is calculated as follows:

$$\overline{P}_{\text{year},k} = \sum_{j=1}^{N_w} \left[\left(\frac{H_j}{2} \right)^2 \times P_k(T_j) \times S_j \right] \tag{9}$$

where H_j, T_j, and S_j denote the mean wave height, mean wave period, and occurrence probability of the j-th wave component in the joint probability distribution, respectively. N_w is the total number of wave components. In the linear irregular wave theory, if the wave heights are assumed to follow a Rayleigh distribution, the significant wave height $H_{s,j}$ and the mean wave height H_j shown in Fig. 4 can be converted:

$$H_j = \sqrt{\frac{\pi}{8}} H_{s,j} \tag{10}$$

The total wave power $P_{\text{total}}(T)$ and the annual average power generation $\overline{P}_{\text{year}}$ of the hybrid system are obtained by summing the contributions of all WECs:

$$P_{\text{total}}(T_j) = \sum_{k}^{3} P_k(T_j) \tag{11}$$

$$\overline{P}_{\text{year}} = \sum_{k}^{3} \overline{P}_{\text{year},k} \tag{12}$$

3.3. Optimization algorithm

Genetic algorithm (GA) is a widely used optimization method, showing notable advantages in global optimization and in addressing problems lacking explicit mathematical models (Lambora et al., 2019). The basic principle of GA is inspired by Darwin's natural selection and genetic concepts, where the population evolves iteratively through operations such as selection, crossover, and mutation, gradually approaching the optimal solution (Gunantara, 2018). NSGA-II is a multi-objective optimization algorithm known for its superior performance in handling complex optimization problems and has been widely used in various engineering and scientific fields (Huang et al., 2024) (Huang et al., 2025b). It generates Pareto fronts, representing sets of solutions where no objective can be improved without deteriorating at least one other objective (Huang et al., 2025c). Compared with other optimization algorithms such as Particle Swarm Optimization (PSO) and Simulated Annealing (SA), NSGA-II exhibits strong capability in maintaining solution diversity and generating well-distributed Pareto solutions without requiring additional weighting factors (Deb et al., 2002). In this study, NSGA-II is applied to address the optimization problem, and the framework of the optimization process is shown in Fig. 6.

The optimization objectives of the hybrid system are to enhance

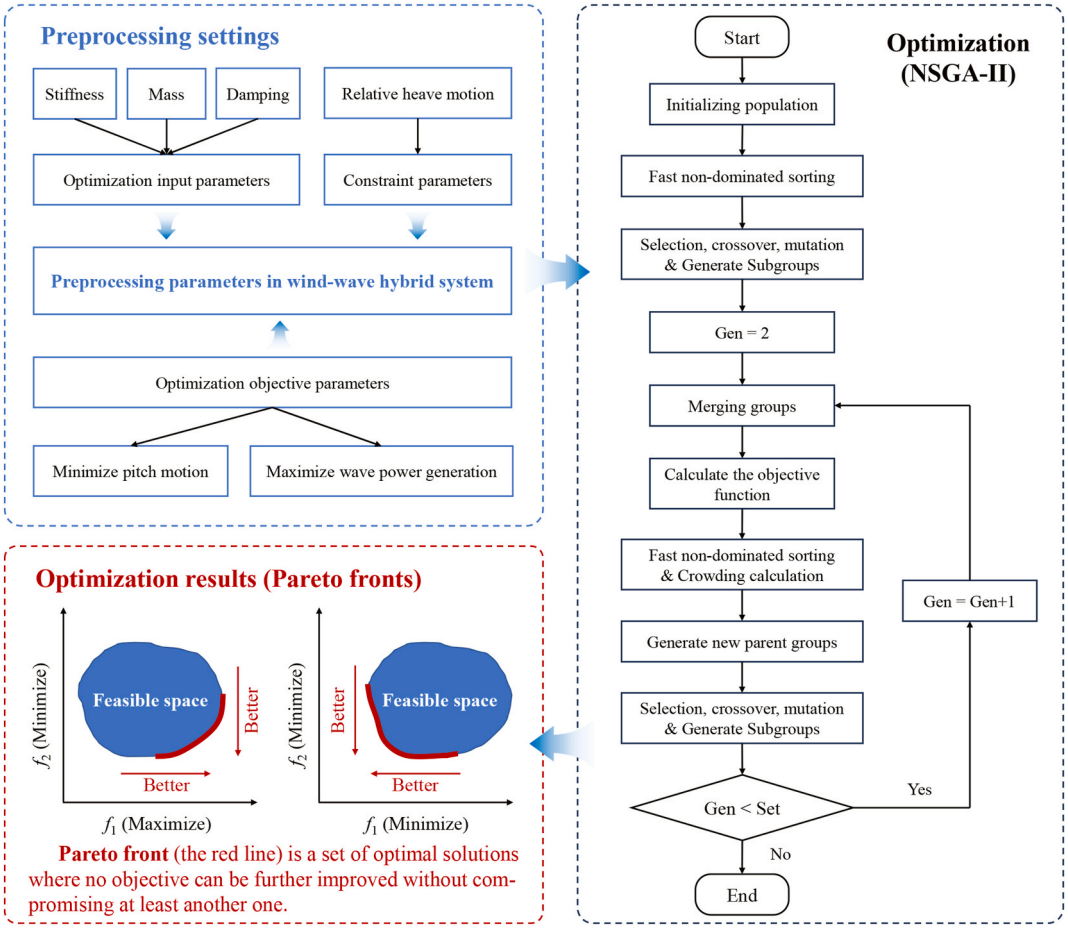

Fig. 6. The framework of the optimization process.

wave power generation and to reduce platform pitch motion. Specific optimization indices under different strategies will be presented in the following sections. In addition, the maximum relative heave peak value $z_{r,max}$ is constrained to not exceed 10 m. For all cases, the initial population size is set to 30, the number of generations to 100 (with some cases extended to 150 depending on convergence), the crossover probability to 0.9, and the mutation probability to 0.1. The initial population is generated using the uniform Latin hypercube (ULH) method. Unlike the classical Latin hypercube, which usually ensures a correct distribution only for continuous input variables, ULH can also produce a proper uniform distribution for discrete variables (McKay et al., 1979). The distribution of the initial points generated by the ULH method in this study is provided in Fig. 7, demonstrating a good distribution with a relatively small number of points. This sampling strategy is particularly suitable for producing initial datasets for optimization with genetic algorithms.

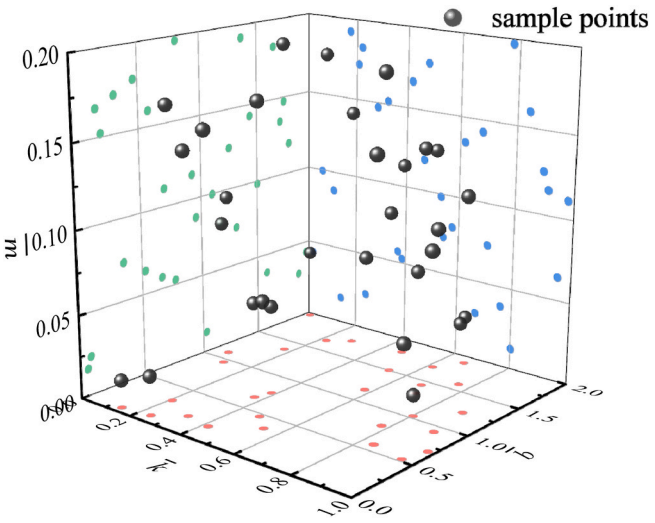

Fig. 7. The distribution of the initial points generated by the ULH method.

3.4. Numerical model validation

The present model is validated against the widely applied open-source time-domain program WEC-Sim, developed by the National Renewable Energy Laboratory (NREL) and Sandia National Laboratories (SNL) (Ruehl et al., 2014). The response amplitude operators (*RAOs*) of the floating platform and the built-in WECs are compared, which are obtained by normalizing the motion amplitudes with the incident wave amplitude at each period. For the validation case, the dimensionless mass, stiffness, and damping coefficients of the WECs are set to 0.423, 0.177, and 0.170, respectively. The comparison results show that the overall trends of the *RAOs* calculated by the present model agree well with those obtained from WEC-Sim (Fig. 8). The maximum relative error in platform pitch motion does not exceed 7.5%, while the relative errors in the other degrees of freedom are consistently smaller, indicating good overall agreement between the two models. These results demonstrate that the motion responses of both the platform and the built-in WECs can be reliably calculated by the present model.

4. Multi-objective optimization analysis

4.1. Determination of optimization strategies

This subsection focuses on optimization strategy design rather than parameter tuning, comparing two approaches to examine how different sea-state definitions influence the robustness and engineering relevance of PTO system optimization results: one based on a single representative sea state, and the other conducted over a range of operational sea states.

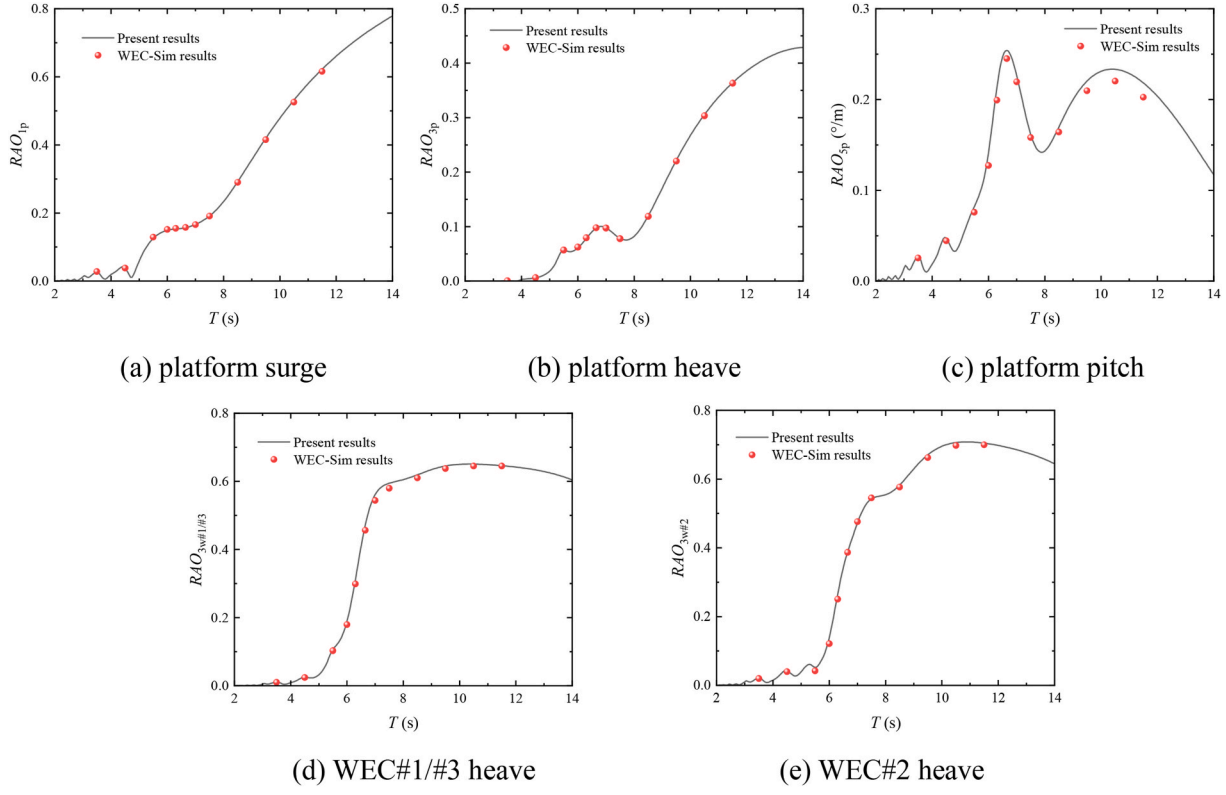

Fig. 8. Model validation through comparison of motions between the present model and WEC-Sim.

4.1.1. Optimization based on a single representative sea state

In the first optimization strategy (Case A), the representative sea state with the highest occurrence probability in the joint probability distribution (T = 5.5 s, H_s = 1.25 m) is adopted as the regular wave input, while minimizing the pitch motion peak and maximizing the total power generation are set as the optimization objectives. Fig. 9 presents the results of this optimization strategy, including the dynamic responses and power performance of selected optimal solutions under a unit wave amplitude.

In Fig. 9a, the black squares represent the initial design-of-experiments (DOE) population generated within the prescribed design-variable ranges using the ULH sampling method. This initial population is adopted as the starting point of the NSGA-II multi-objective optimization, in which offspring populations were iteratively generated through non-dominated sorting, crowding-distance-based selection, and genetic operators including crossover and mutation. The evaluated offspring populations are denoted by the blue circles. The optimization process is terminated when the Pareto front exhibits negligible improvement between successive generations, and the final Pareto front is extracted from all evaluated offspring populations, as indicated by the red circles in Fig. 9a. It is observed that the initial population is mainly concentrated in the lower-left region, corresponding to smaller pitch responses and lower total power generation. In contrast, the obtained Pareto front gradually shifts toward solutions with higher power generation, which are generally accompanied by increased pitch responses, or alternatively toward reduced motion responses at the expense of power generation. This indicates a clear trade-off between power generation and platform stability, where improvements in energy extraction tend to amplify platform motions due to the enhanced energy dissipation introduced by the PTO system. Therefore, the Pareto solutions represent different optimal compromises between energy harvesting performance and motion suppression capability.

Four representative solutions are selected from the Pareto front, with the pitch responses not exceeding the single-platform motion peak value under the representative sea state (3.86×10^{-2} deg) (the selection of representative solutions hereafter follows the same rule), and are labeled as Case A1 to Case A4 for further performance analysis (Fig. 9a). The corresponding PTO parameters, pitch response peak values, and total power generation are listed in Table 6. It is observed that the dimensionless stiffness gradually decreases with increasing case number, while the dimensionless mass remains close to the upper bound of the prescribed range.

As shown in Fig. 9b and c, new resonant peaks induced by the PTO appear in both heave and pitch directions within the short-period range. It is noteworthy that the integration of the heave oscillating body WECs also leads to a new coupled resonant peak in the pitch response of the platform. This phenomenon arises because the WECs are installed away from the platform's center of gravity, such that their heave motion alters

Table 6
The optimal PTO parameters under representative sea conditions.

Case	$\bar{k}$	$\bar{b}$	$\bar{m}$	θ (deg)	P_{total} (kW)
Case A1	0.905	0.010	0.181	2.859×10^{-4}	1.808×10^{-1}
Case A2	0.843	0.187	0.197	1.002×10^{-2}	6.226×10^{1}
Case A3	0.766	0.107	0.199	2.306×10^{-2}	1.346×10^{1}
Case A4	0.737	0.043	0.199	3.840×10^{-2}	2.061×10^{1}

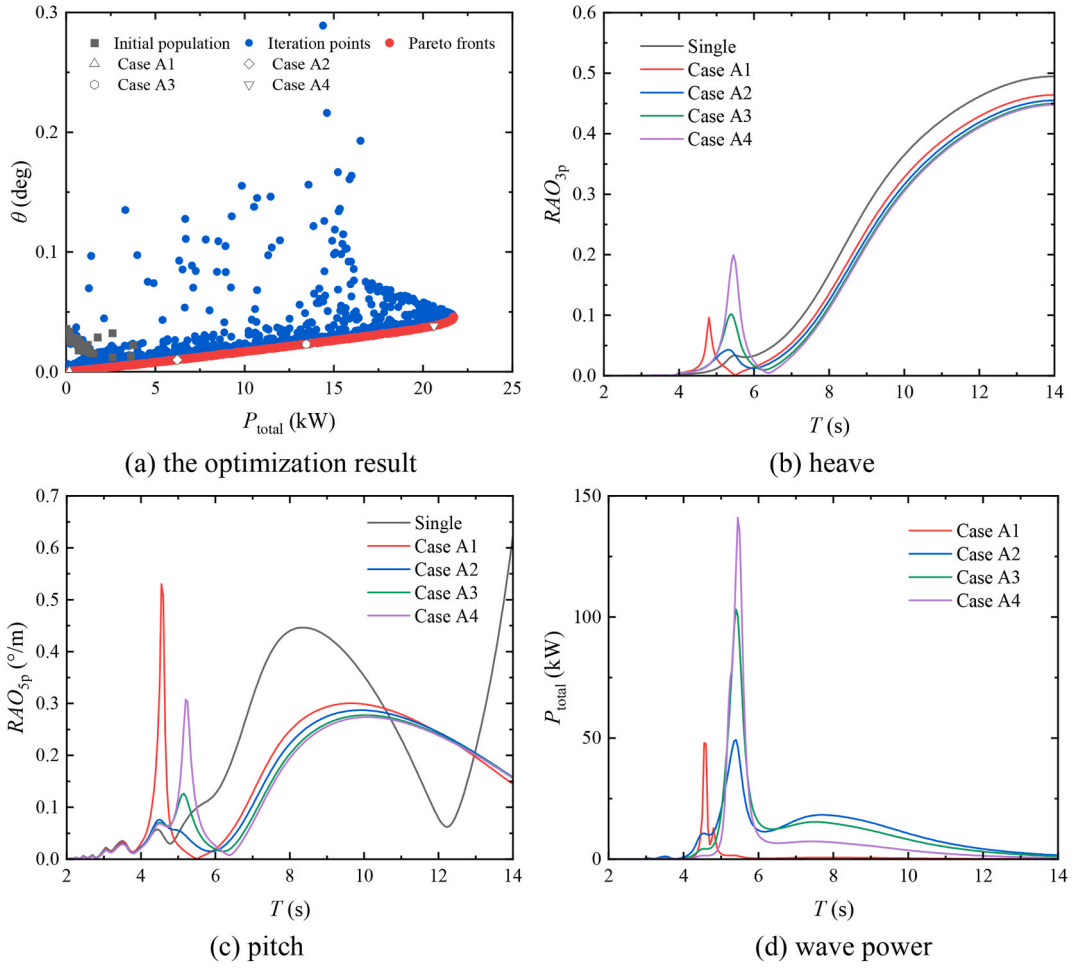

Fig. 9. Multi-objective optimization results and hybrid system performance under representative sea conditions.

the original pitch response of the platform through moment coupling and disturbance of the restoring force. Moreover, since the WECs are distributed on the side columns of the platform and inherently include damping components rather than behaving as ideal oscillators, the actual resonant periods generally deviate from those calculated by the theoretical vibration model.

In the pitch direction, the resonant peak value shows no clear correspondence with the case order. However, it can be observed that with increasing case order, the PTO resonant period gradually approaches the representative period, resulting in smaller response attenuation at this period and thus causing differences in pitch peak values among cases. Relatively large resonant peaks in the short-period range are exhibited in Case A1 and Case A4, which may trigger abnormally high motion responses of the system.

In the period range following the resonance, the heave responses of all four cases remain lower than that of the single platform. In the pitch direction, the introduction of the WECs smooths the original peak profile of the single platform motion, significantly reducing its maximum peak value, while the attenuation of the peak profile extends over a slightly wider range of wave periods. Overall, the pitch responses are substantially reduced compared with the single platform, except in the short-period range due to the delayed attenuation of the peak profile. Fig. 9d further illustrates the variation of power generation with wave period. For Case A1, the power peak occurs on the left side of the representative period, resulting in extremely low power generation at the representative period. In contrast, the power peaks of the other three cases (Case A2-Case A4) are concentrated near the representative period, with energy absorption mainly occurring over a relatively narrow period range.

4.1.2. Optimization based on a range of operational sea states

The second optimization strategy (Case B) focuses on the range of operational sea states selected based on a cumulative probability of 99% from the joint probability distribution (the effect of different cumulative probabilities is discussed in the next section). Similar cumulative probability values are widely adopted in the sea state limit design of many offshore engineering projects (Det Norske Veritas (DNV), 2010) (Det Norske Veritas (DNV), 2011). The selection procedure of the operational sea state range in this study is as follows: the two-dimensional joint probability distribution of wave height and period is sorted in descending order of probability density. By cumulatively summing the probabilities of each sea state combination, the first set of sea states that together reach 99% cumulative probability is identified. Among these selected sea states, the maximum wave height and maximum wave period are extracted, and the rectangular region defined by this maximum wave height and maximum period is taken as the operational sea state (excluding the initial columns where the probability of occurrence is zero), as illustrated in Fig. 4. Compared with probability contours, the rectangular boundary is somewhat conservative because it includes sea states that rarely occur, while contour-based selection, although more precise, can be inconvenient due to its irregular boundary and the difficulty of selecting discrete sea states within the contour. The rectangular boundary is adopted here for its simplicity and ease of implementation.

Within this operational sea state, the WECs operate normally. Sea states beyond this range are defined as extreme conditions, under which the WECs cease operation and do not contribute to power generation (Zhou et al., 2024). Therefore, they are not considered in the multi-objective optimization. Case B optimization is performed based on the operational sea state, with the dual objectives of minimizing the

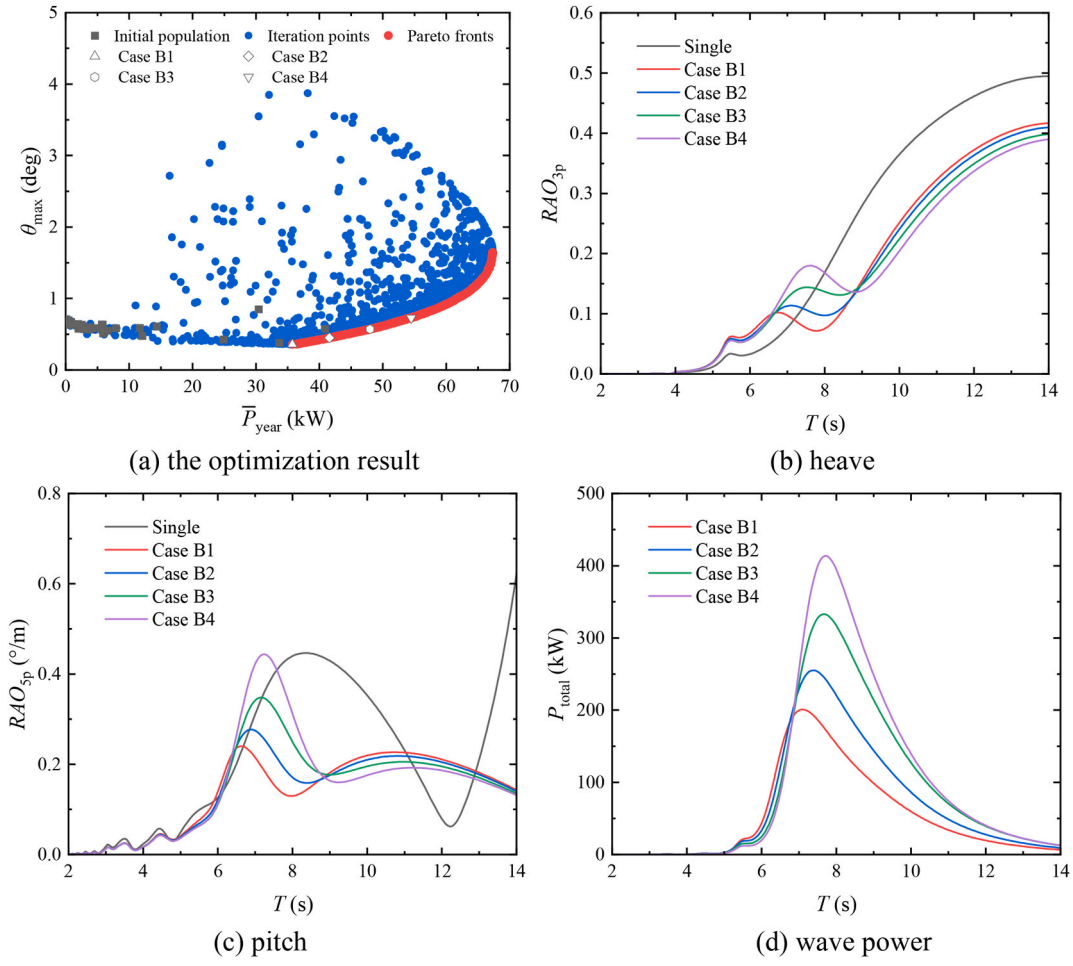

Fig. 10. Multi-objective optimization results and hybrid system performance under operating sea condition (99%).

maximum platform pitch motion and maximizing the annual average power generation.

Fig. 10 presents the optimization results and the selected representative optimal solutions, showing the variations of system motion responses and power performance with wave period under a unit wave amplitude. Consistent with the previous approach, four representative solutions are extracted from the Pareto front shown in Fig. 10a, where the maximum pitch motion within the operational sea states does not exceed that of the single platform (0.733°). These solutions are denoted as Case B1 to Case B4. The corresponding PTO parameters, maximum pitch motion, and annual average power generation are summarized in Table 7. In Case B1, the maximum pitch motion θ_{max} is 0.359°, reduced by approximately 51.02% compared with the single platform, showing significant attenuation of pitch motion. Like Case A, the dimensionless stiffness decreases progressively with the case increase. The dimensionless mass is consistently taken at the upper bound of the prescribed range, with the dimensionless damping showing little variation across the cases, all ranging between 0.2 and 0.3. This boundary tendency is attributed to the beneficial inertial effect of increased mass on system performance, while the upper bound is defined by the maximum mass that can be accommodated within the internal space. Such a boundary tendency reflects practical design constraints and does not affect the validity of the obtained optimal solutions under the defined parameter bounds.

It can be observed that compared with Case A, the PTO resonant peaks in Case B no longer exhibit sharp features and become smoother (Fig. 10b and c). Moreover, as the case increases, both the resonant peak values and periods in heave and pitch show an upward trend. In the heave direction, the motion response of the hybrid system is slightly higher than that of the single platform in the short-period range, while only in the period range beyond the resonant period does it demonstrate a suppression effect compared to the single platform, with this effect being more pronounced than that in Case A.

Specifically, under the operational sea state, the maximum heave motion of the hybrid system z_{max} occurs in Case B1 at the wave height-period combination ($T = 10.5$ s, $H_s = 5.25$ m), with a value of 0.424 m, which is lower than the maximum value of 0.593 m observed for the single platform at the combination ($T = 10.5$ s, $H_s = 5.25$ m). For the pitch response, except near the PTO resonant period and in the short-period range influenced by the delayed attenuation of the original peak of the single platform, the response peak values of the hybrid system remain generally lower than those of the single platform across the rest of the period range. Compared with Case A, the period range affected by the delayed attenuation of the original peak becomes even shorter. Fig. 10d indicates that stable energy absorption is achieved across a relatively wide period range, corresponding to the multi-objective optimization target of annual average power generation.

Overall, compared with Case A, the optimization adopted in Case B is more comprehensive in its objective settings, as it not only accounts for the system response characteristics under the overall operational sea states but also effectively reduces the maximum pitch peak value. Meanwhile, it broadens the effective frequency bandwidth for wave energy absorption, thereby significantly mitigating the risk of extreme motion responses within certain period ranges caused by optimization targeting a single representative sea state.

Table 7
The optimal PTO parameters under operating sea conditions (99%).

Case	$\bar{k}$	$\bar{b}$	$\bar{m}$	θ_{max} (deg)	$\bar{P}_{year}$ (kW)
Case B1	0.487	0.207	0.200	0.359	35.73
Case B2	0.452	0.244	0.200	0.451	41.58
Case B3	0.407	0.263	0.200	0.571	47.97
Case B4	0.383	0.219	0.200	0.728	54.49

4.1.3. *Convergence and local robustness analysis*

To assess the convergence characteristics of the multi-objective optimization, a systematic analysis is conducted using Case B by examining the evolution of the Pareto front over successive iterations, as shown in Fig. 11. The results indicate that the Pareto front approaches a

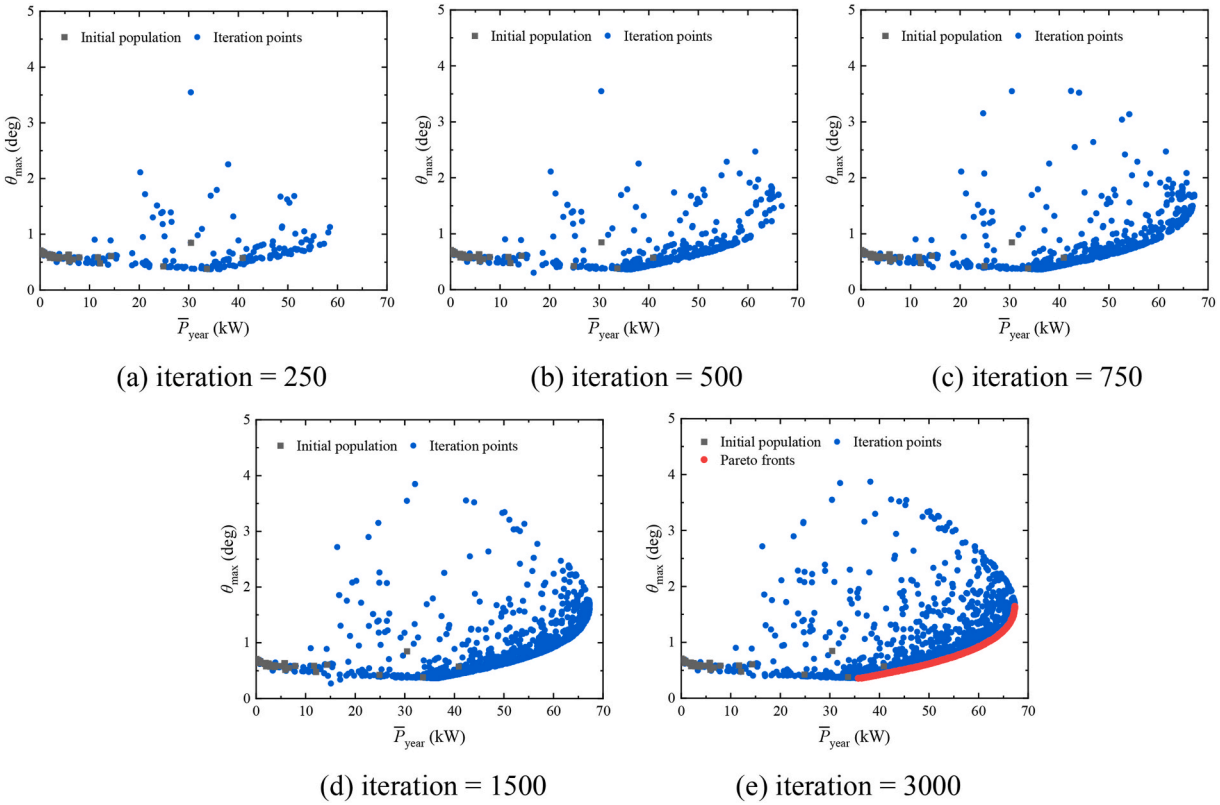

Fig. 11. The convergence behavior of the multi-objective optimization process.

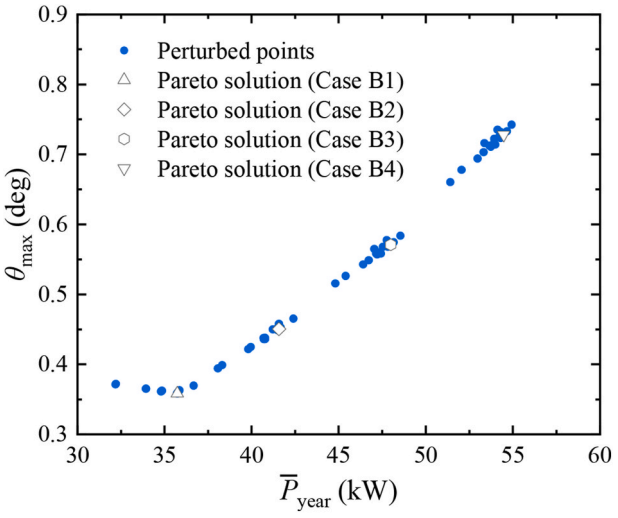

Fig. 12. The comparison of optimized Pareto solutions and perturbed points.

stable configuration after approximately 1500 iterations, with only marginal changes observed thereafter. Nevertheless, the optimization is continued up to 3000 iterations to ensure the robustness and stability of the final solution set and to reduce the risk of premature convergence. These observations confirm that the optimization has effectively converged, and the obtained Pareto-optimal solutions can be considered reliable.

To further evaluate the quality and robustness of these solutions, a local perturbation analysis is conducted around four representative Pareto-optimal points from Case B. For each solution, small perturbations are applied around the optimized parameter values of $\overline{k}$, $\overline{b}$, and $\overline{m}$ to generate nearby points for verification. Two types of perturbations are considered: (1) simultaneous perturbations of all three parameters with ± 0.5 %, ± 1 %, and ± 2 % for $\overline{k}$ and $\overline{b}$, whereas $\overline{m}$ being close to its upper bound, is only decreased by the same percentages; and (2) single-parameter perturbations, where each parameter is individually perturbed by $\pm$ 1 %. The objective function values of all perturbed points are evaluated and compared with the original Pareto solutions, as shown in Fig. 12. The results show that none of the perturbed points, whether from simultaneous or single-parameter perturbations, simultaneously improved both objectives (minimizing the maximum platform pitch motion and maximizing the annual average power generation). This confirms that the original Pareto solutions are locally optimal within the considered perturbation range, demonstrating the robustness and effectiveness of the NSGA-II optimization results.

4.2. Comparison of different operational sea states

Three sets of typical operational sea states defined by different cumulative probabilities are compared. The previous section has introduced the method of defining operational sea states based on cumulative probability, where the sea state corresponding to the 99% cumulative probability was considered, and the superiority of the corresponding optimization strategy was verified. To further discuss the influence of

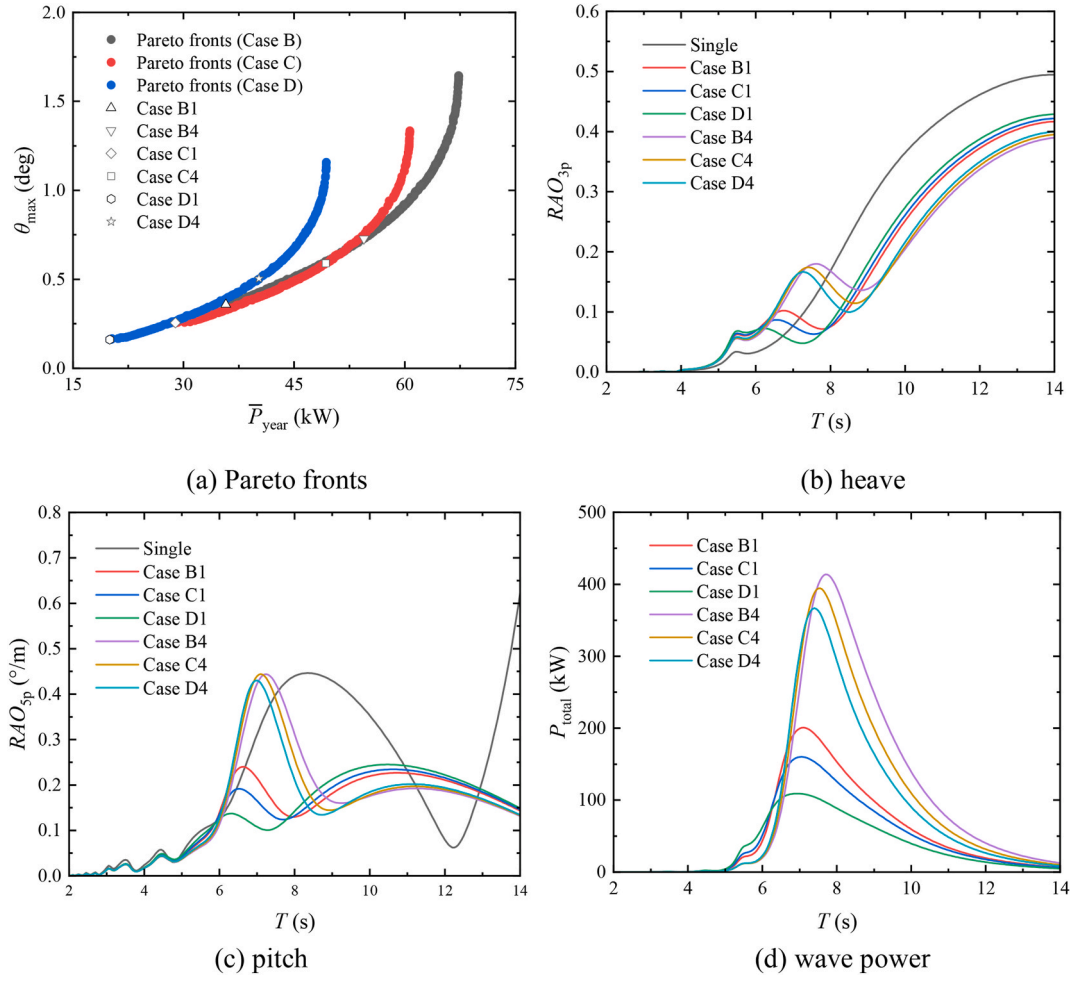

Fig. 13. The comparison of multi-objective optimization results and hybrid system performance under different defined operating sea conditions.

cumulative probability on the optimization results, two additional sets of typical operational sea states are selected, corresponding to 95% (Case C) and 90% (Case D) cumulative probability, as also shown in Fig. 4.

Fig. 13a compares the optimal solution sets obtained under the three representative operational sea states. From each set, two representative solutions are selected, whose maximum pitch responses within the corresponding operational sea state remain lower than that of the single platform (0.733°, 0.593°, and 0.513°, respectively). The PTO parameters, maximum pitch responses, and annual average power generation of these representative solutions are summarized in Table 8. The results indicate that the maximum pitch peak value θ_{max} of Cases B1 to D1 is reduced by approximately 51.02%, 56.83%, and 68.62% compared with the single platform, showing an increasing attenuation of pitch response. With the decrease in cumulative probability, more sea states with large wave heights or long wave periods are excluded, which leads to a further reduction in the maximum pitch response. Meanwhile, the upper limit of the annual average power generation of the hybrid system also shows a corresponding decreasing trend.

Table 8
The optimal PTO parameters under different defined operating sea conditions.

Case	$\bar{k}$	$\bar{b}$	$\bar{m}$	θ_{max} (deg)	$\bar{P}_{year}$ (kW)
Case B1	0.487	0.207	0.200	0.359	35.73
Case C1	0.514	0.218	0.200	0.256	28.88
Case D1	0.560	0.214	0.200	0.161	20.00
Case B4	0.383	0.219	0.200	0.728	54.49
Case C4	0.398	0.192	0.199	0.589	49.27
Case D4	0.411	0.178	0.198	0.504	40.24

Meanwhile, Fig. 13b, c, d presents a comparison of the variations in system motion responses and total power generation with wave period under a unit wave amplitude for the representative solutions of each case. It can be observed that, under the operational sea states defined by three different cumulative probabilities, the motion and power generation curves of the hybrid system exhibit similar overall trends. With the decrease of cumulative probability, the resonant period and PTO resonant peak are reduced in order to adapt to shorter-period sea states. This change in resonant period is also reflected in the gradual reduction of dimensionless stiffness in Table 8, while the dimensionless mass remains nearly unchanged and consistently stays at the upper limit of its range.

Although some numerical differences exist in the optimized results under different operational sea states defined by cumulative probability, the overall optimization trend remains consistent, without altering the fundamental law of motion response and power performance of the hybrid system. This indicates that the system optimization based on the overall operational sea state is highly reliable and is not significantly affected by the specific definition of the sea state. Therefore, in practical engineering applications, a reasonable working sea state can be flexibly selected as the basis for optimization according to the actual sea area conditions.

4.3. Trade-off between power and mass

As revealed by the previous analysis, the multi-objective optimization considering maximum power generation and minimum platform pitch has brought the system performance close to its achievable opti-

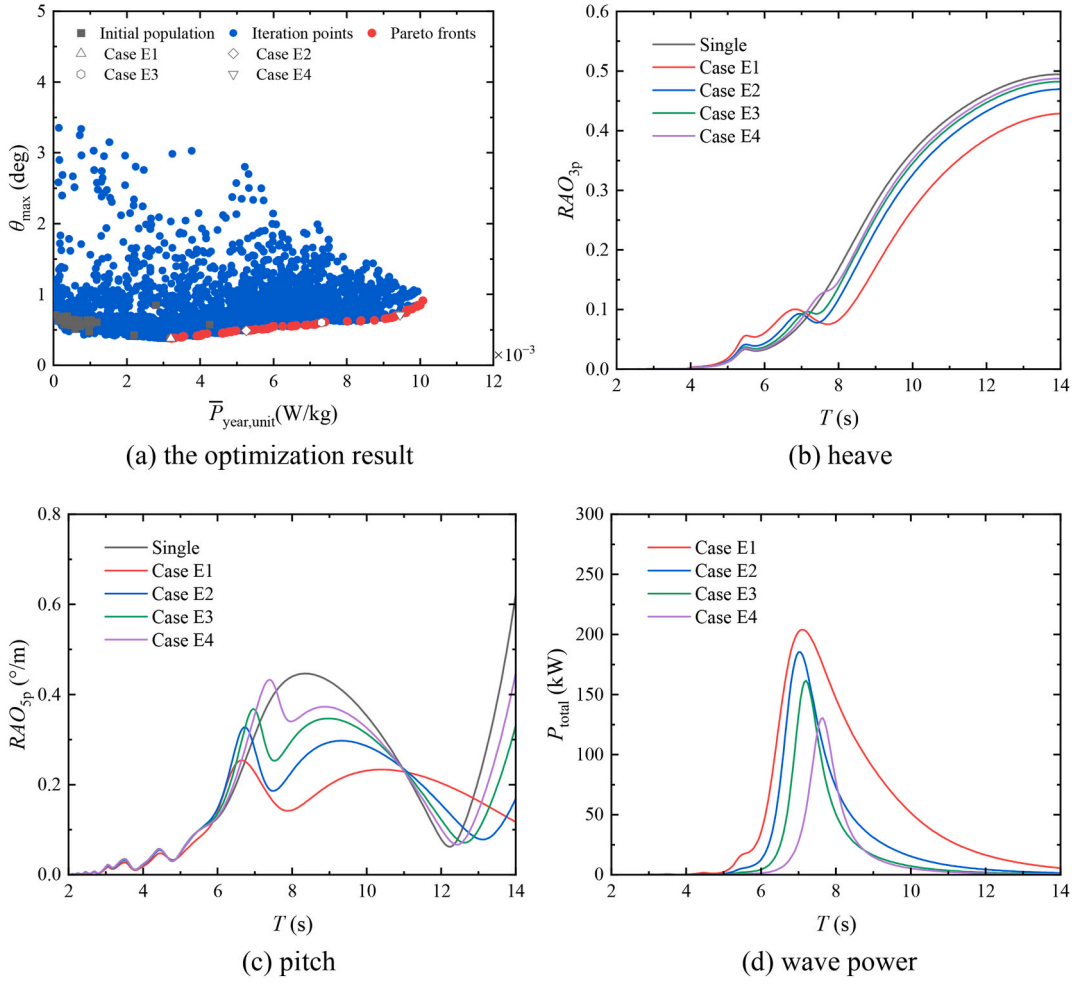

Fig. 14. Multi-objective optimization results and hybrid system performance after optimizing $\bar{P}_{year,\ unit}$.

mum. To further expand the evaluation dimension and provide a more comprehensive reflection of the trade-off between power generation and structural mass, thereby offering additional references for engineering applications, a new performance evaluation indicator, referred to as the annual average power generation per unit mass ($\overline{P}_{\text{year, unit}}$) (Zhang et al., 2025), is further introduced to replace the original power generation indicator. Its definition is given as follows:

$$\overline{P}_{\text{year,unit}} = \frac{\overline{P}_{\text{year}}}{m_{\text{wec,total}}} \tag{13}$$

In this section, the operational sea states with a cumulative probability of 99% are again adopted, within which a multi-objective optimization is carried out considering both the $\theta_{\max}$ and $\overline{P}_{\text{year, unit}}$. The optimization results are presented in Fig. 14, together with the motion responses and power performance of several representative optimal solutions under a unit wave amplitude. The corresponding PTO parameters, maximum pitch motion, and $\overline{P}_{\text{year, unit}}$ are summarized in Table 9.

With the increase in the case, the dimensionless mass, stiffness, and damping gradually decrease, while the heave resonant period of the system correspondingly increases. Compared with the results of Case B, Case E exhibits smaller variations in the heave motion of the single platform across different cases, leading to responses that are closer to the motion characteristics of the single platform. This trend becomes more pronounced in larger cases. In the pitch direction, both the PTO resonant peak and resonant period increase with the case. Relative to Case B, the PTO resonant peak profile of Case E is narrower and transitions more rapidly toward the platform inherent resonant peak. As the case increases, the pitch motion response of the system at longer periods becomes closer to that of the single platform, while the period range of pitch amplification, which is caused by the delayed attenuation of the platform's inherent resonant peak, becomes narrower. However, the corresponding motion-reduction effect is also weakened.

Fig. 15 compares the $\theta_{\max}$ and $\overline{P}_{\text{year, unit}}$ for selected optimal solutions in Cases B and E. While the pitch attenuation remains nearly unchanged, the annual average power generation per unit mass is significantly increased, reaching a 119.39% improvement in Case E4. This result indicates that, under the constraint of platform motion performance, optimizing the PTO parameters using the indicator $\overline{P}_{\text{year, unit}}$ can effectively enhance the system's economic performance and energy usage efficiency.

Under this optimization strategy, the maximum pitch motion of the hybrid system in the given sea state can be reduced by up to 48.29% compared with the single platform. The WECs can achieve a peak power generation of 204.08 kW under a unit wave amplitude conditions, and $\overline{P}_{\text{year, unit}}$ can reach up to 9.59×10^{-3} W/kg. This optimization strategy also provides four representative sets of optimal solutions, which can be flexibly selected in practical engineering applications according to whether the system prioritizes power generation performance or motion reduction performance, together with the corresponding parameter configurations.

Table 9
PTO parameters optimized for $\overline{P}_{\text{year, unit}}$.

Case	$\overline{k}$	$\overline{b}$	$\overline{m}$	$\theta_{\max}$ (deg)	$\overline{P}_{\text{year, unit}}$ (W/kg)
Case E1	0.423	0.177	0.170	0.378	3.20×10^{-3}
Case E2	0.188	0.054	0.068	0.488	5.26×10^{-3}
Case E3	0.090	0.022	0.033	0.602	7.31×10^{-3}
Case E4	0.041	0.010	0.016	0.711	9.45×10^{-3}

5. Influence of PTO parameters on system performance

In the previous chapter, a multi-objective optimization is conducted for the three PTO parameters of the hybrid system, resulting in several relatively comprehensive sets of optimal solutions. However, the specific influences of each PTO parameter on system performance remain unclear, and the optimization process still exhibits certain "black-box" characteristics. Therefore, one representative optimal solution from Case E in the final iteration, namely Case E1, is selected as a reference case. Case E1 is chosen from the motion-reduction-dominant region of the Pareto front, representing a typical optimal solution with relatively strong pitch suppression performance. In addition, the design parameters of Case E1 are not located at the prescribed bounds, which allows sufficient room for parametric variation and facilitates a clear interpretation of the parameter influence mechanisms. It is also noted that the Pareto-optimal solutions obtained under the considered sea-state conditions are generally distributed within a balanced trade-off region, without exhibiting extreme or degenerate parameter combinations, which further supports the representativeness of the selected case for mechanism analysis.

The three dimensionless PTO parameters are individually analyzed to evaluate their effects on the motion responses and power generation performance of the hybrid system. On this basis, further comparisons and discussions of the optimization results are carried out to analyze how variations in PTO parameters along the Pareto front influence the balance between motion reduction and power generation, and to reveal the pitch motion reduction mechanism of the built-in wave energy converters.

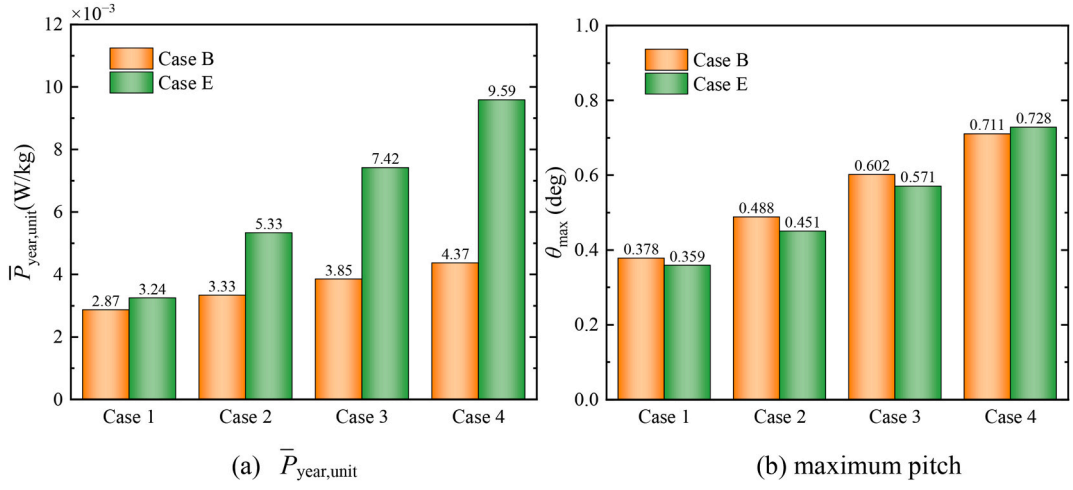

(a) $\overline{P}_{\text{year,unit}}$ (b) maximum pitch

Fig. 15. Comparison of optimization results between Case B and Case E.

5.1. Effect of stiffness

Five PTO parameter sets with varying dimensionless stiffness are designed while keeping the dimensionless damping and mass constant, as summarized in Table 10.

The motion responses and total wave power generation under a unit wave amplitude for different parameter sets at various wave periods are illustrated in Fig. 16. As the stiffness increases, the resonant peak values and periods in the heave and pitch directions are progressively reduced. Correspondingly, both the peak value of the total wave power generation and its associated period are also reduced.

Under the operational sea state defined by the 99% cumulative probability, the statistical results of the maximum pitch and heave motions of the platform, the relative heave motions between the platform and the WECs, as well as the annual average power generation per unit mass are presented in Fig. 17. It is shown that the maximum pitch and heave motions of the platform exhibit a decreasing-increasing trend with the increase in stiffness. This tendency cannot be directly identified from the motion response curves under a unit wave amplitude, as it is caused by the combined effect of the differences in both the resonant peak values and periods among cases, together with the distribution of wave heights corresponding to different periods in the sea state. The annual average power generation per unit mass is also observed to increase first and then decrease with increasing stiffness, reaching its maximum in Case F2.

From Figs. 4 and 16c, it can be inferred that to enhance the annual average power generation, not only should the peak value of the total power generation be increased, but more importantly, the period corresponding to the peak and the overall energy absorption bandwidth should be matched with the target sea state. In addition, the maximum relative heave motion between the platform and the WECs decreases with the increase in stiffness. All the maximum relative heave motions remain within the predefined stroke range of the device, and the maximum relative heave motions on the seaward side are smaller than those on the lee side.

Table 10
PTO parameter settings at different stiffness ($\overline{b}$ = 0.177; $\overline{m}$ = 0.170).

Case	$\overline{k}$
Case F1	0.223
Case F2	0.323
Case F3/Case E1	0.423
Case F4	0.523
Case F5	0.623

5.2. Effect of damping

With the stiffness and mass kept constant, five PTO parameter cases with different damping are specified, as presented in Table 11.

The system motion responses and the total wave power generation

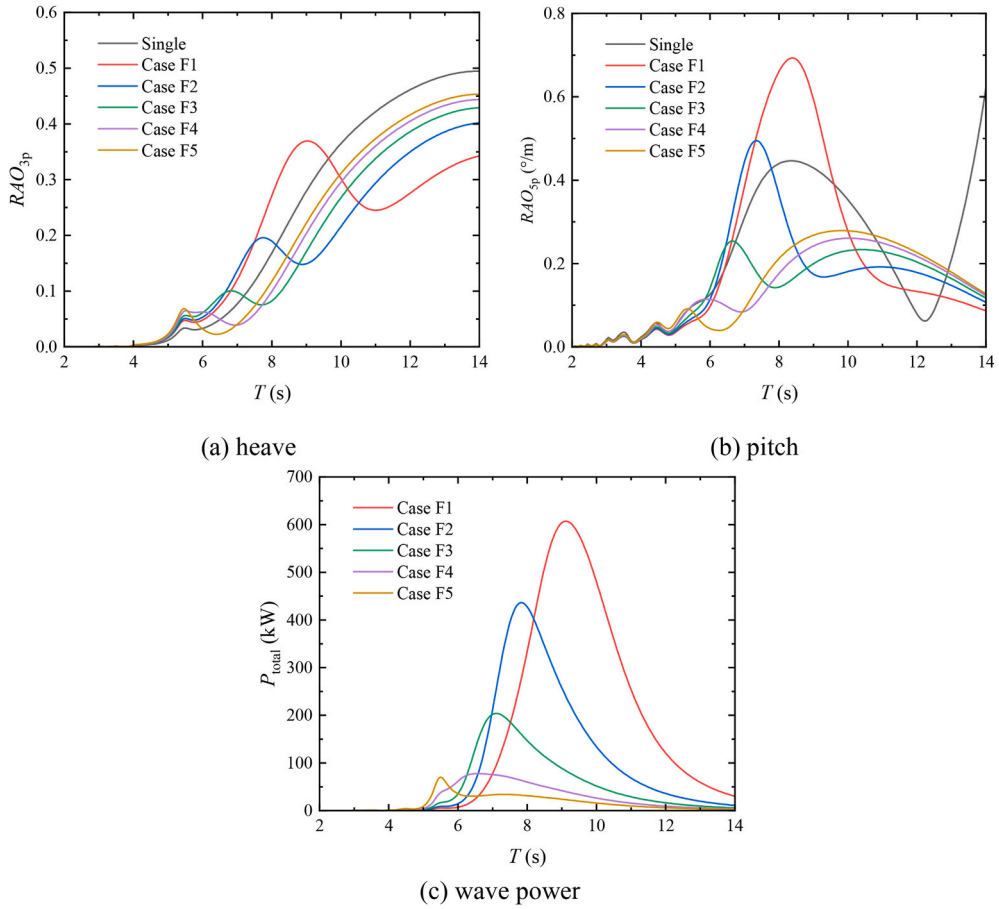

Fig. 16. Hybrid system motion and power performance at different stiffness.

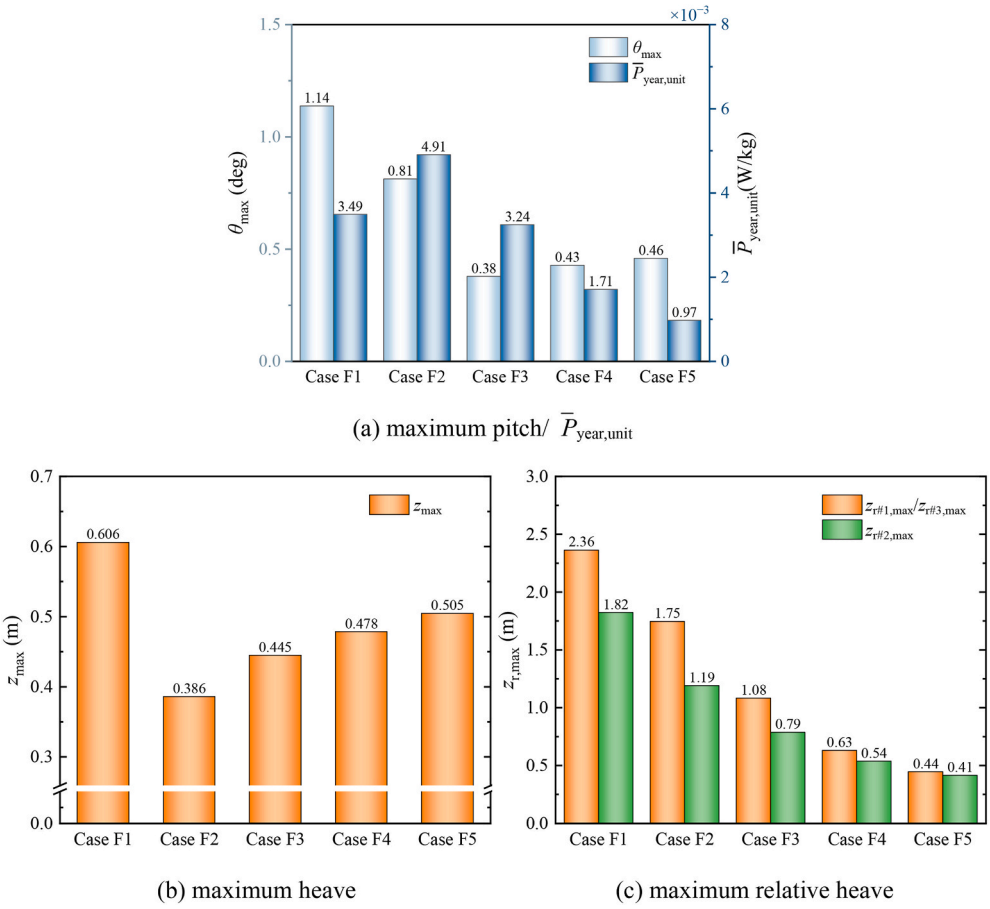

Fig. 17. Hybrid system maximum motion and power at different stiffness.

Table 11
PTO parameter settings at different damping ($\overline{k}$ = 0.423; $\overline{m}$ = 0.170).

Case	$\overline{b}$
Case G1	0.077
Case G2	0.127
Case G3/Case E1	0.177
Case G4	0.227
Case G5	0.277

under a unit wave amplitude at various wave periods are illustrated in Fig. 18 for different parameter cases. With the increase of the damping, the resonant peak values in heave and pitch are gradually reduced, while the corresponding resonant periods are slightly increased. At larger wave periods, the motion response curves remain essentially consistent among the cases, indicating that the influence of damping on the overall motion response is relatively limited, mainly reflected in the adjustment of resonant peaks. The peak value of the total wave power generation decreases with increasing damping, whereas the corresponding peak period becomes larger, accompanied by a broadening of the effective frequency band for energy absorption.

Under the operational sea states defined by the 99% cumulative probability, the statistical results of the maximum pitch and heave motions of the platform, the maximum relative heave motion between the platform and the WECs, and the annual average power generation per unit mass, are presented in Fig. 19. With the increase of the damping, the maximum pitch motion of the platform is observed to decrease initially and then increase, while the annual average power generation per unit mass shows an opposite trend, reaching its maximum at Case G2. The maximum heave motion of the platform is found to increase consistently with damping, whereas the maximum relative heave motion continuously decreases.

5.3. Effect of mass

Five sets of PTO parameter cases with different masses are defined under the condition that the stiffness and damping remain unchanged, as listed in Table 12.

The system motion responses and the total wave power generation under a unit wave amplitude, with respect to the wave period for different parameter cases, are shown in Fig. 20. With the increase of the mass, both the resonant peak values and the resonant periods of the platform in the heave and pitch directions increase, while the peak value of the total wave power generation and its corresponding peak period are also enhanced. Overall, the influence of increasing mass on the integrated system is similar to that of decreasing the PTO stiffness. In addition, although the actual resonant period usually deviates from that calculated by the theoretical vibration model, a positive correlation with the ratio of mass to stiffness is still observed.

Under the operational sea state defined by the 99% cumulative probability, the statistical results of the maximum pitch, heave, and

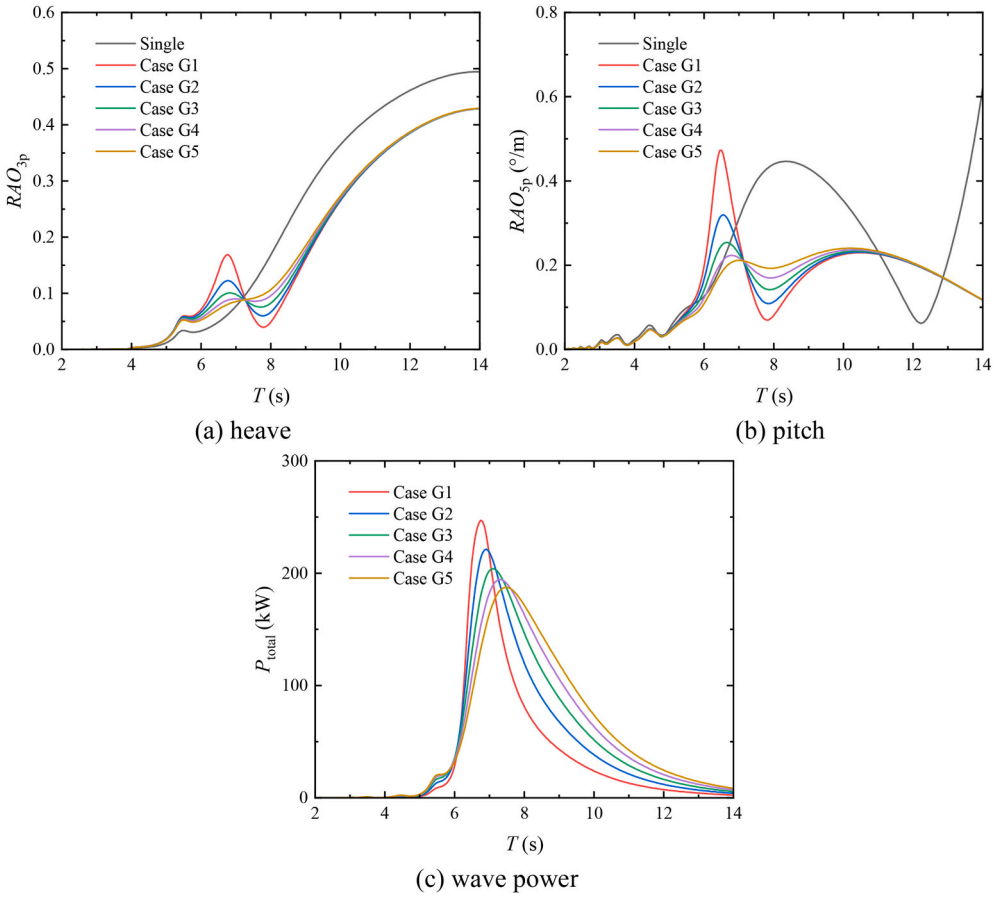

Fig. 18. Hybrid system motion and power performance at different damping.

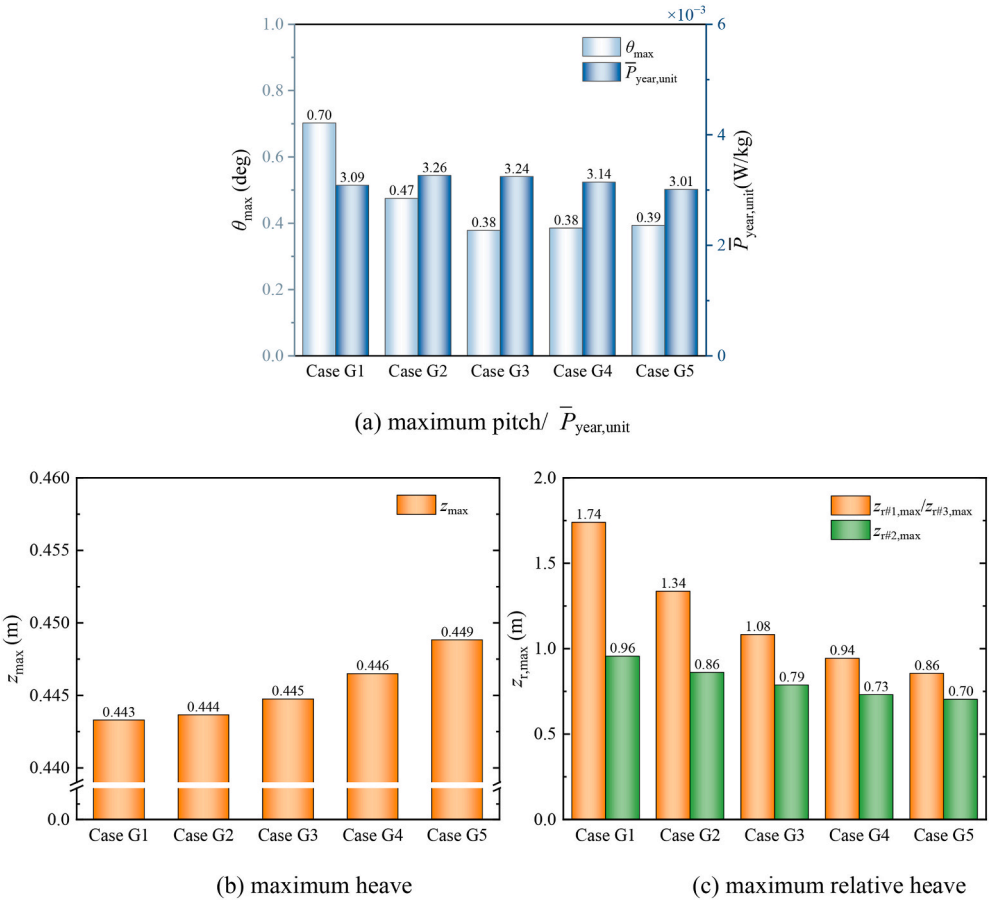

Fig. 19. Hybrid system maximum motion and power at different damping.

Table 12
PTO parameter settings at different mass ($\bar{k}$ = 0.423; $\bar{b}$ = 0.177).

Case	$\bar{m}$
Case H1	0.080
Case H2	0.110
Case H3	0.140
Case H4/Case E1	0.170
Case H5	0.200

relative heave motion between the platform and the WECs, as well as the annual average power generation per unit mass, are presented in Fig. 21. With the increase in mass, the maximum pitch motion of the platform first decreases and then increases, while both the annual average power generation and the annual average power generation per unit mass continuously increase. The maximum heave motion of the platform decreases monotonically with increasing mass, whereas the maximum relative heave motion gradually increases. Consistent with the results obtained for different stiffness and damping, the maximum relative heave motion of all cases is effectively constrained within the preset stroke range of the device, and the maximum relative heave motion of the WEC on the seaward side is always smaller than that on the lee side.

5.4. Underlying mechanisms and implications

In the preceding sections, the effects of three different PTO parameters on the hybrid system are investigated. Variations in PTO stiffness and mass mainly influence the resonant peak values and corresponding periods of pitch and heave motions, as well as the peak power generation and its associated period. The increase in mass and the decrease in PTO stiffness exhibit similar effects on the hybrid system. In contrast, variations in PTO damping mainly modulate the resonant peak values of pitch and heave motions, while having a relatively minor effect on the corresponding resonant periods. At the same time, PTO damping significantly affects the bandwidth of the energy absorption for wave power generation.

For the multi-objective optimization cases targeting maximum pitch motion and annual average power generation (or annual power generation per unit mass), namely Case B and Case E, Case B1 and Case E1 represent the solutions exhibiting the smallest maximum pitch motion within their respective Pareto fronts. To achieve effective suppression of the maximum pitch motion, the primary requirement is to shift the PTO resonant period in the pitch direction away from the wave periods associated with large wave heights within the operational sea state. From the perspective of the probability distribution, to maximize wave power generation while maintaining motion reduction, the PTO resonant period in the heave direction should be shifted toward the shorter-period range of the operational sea state. Moreover, for both Case B and Case E, Cases 1 to 4 essentially reflect different trade-offs between power generation and motion reduction within the Pareto front. During the transition from solutions emphasizing motion reduction to those prioritizing power generation, the PTO resonant periods gradually increase. These variations are determined by the adjustment of the ratio of mass to stiffness and require appropriate damping to achieve optimal power generation performance.

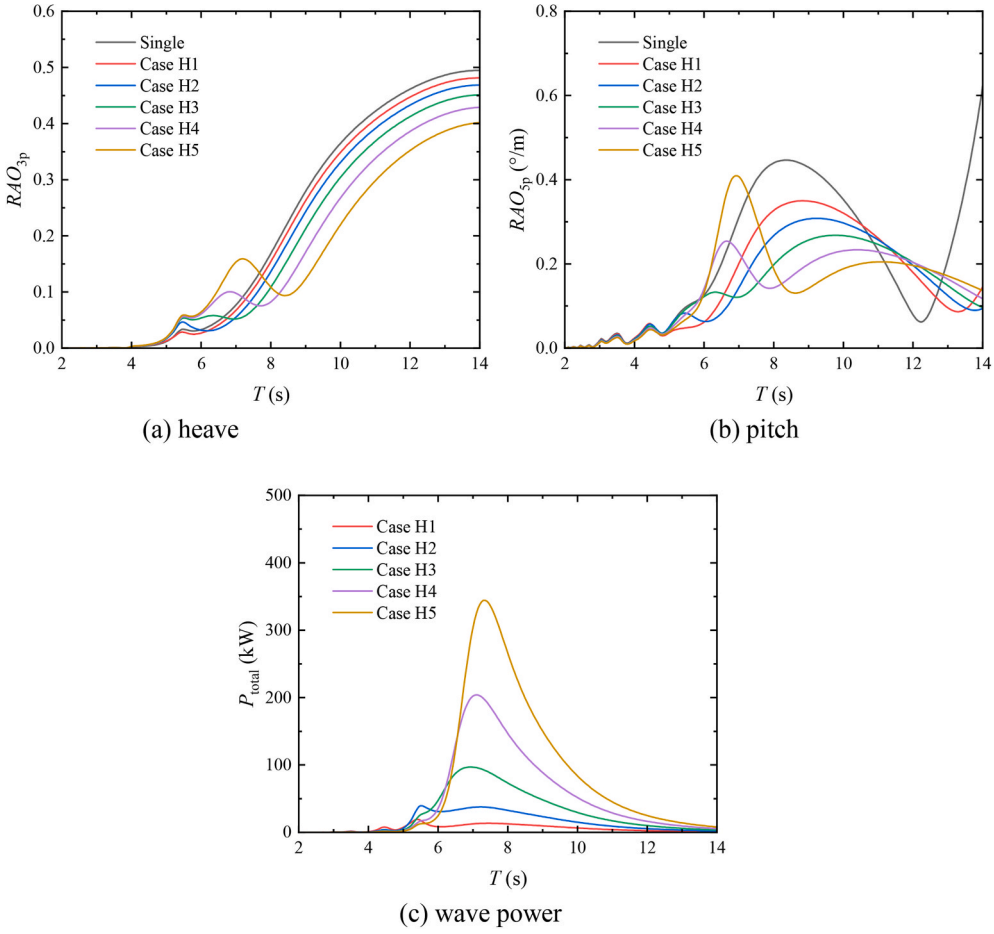

Fig. 20. Hybrid system motion and power performance at different masses.

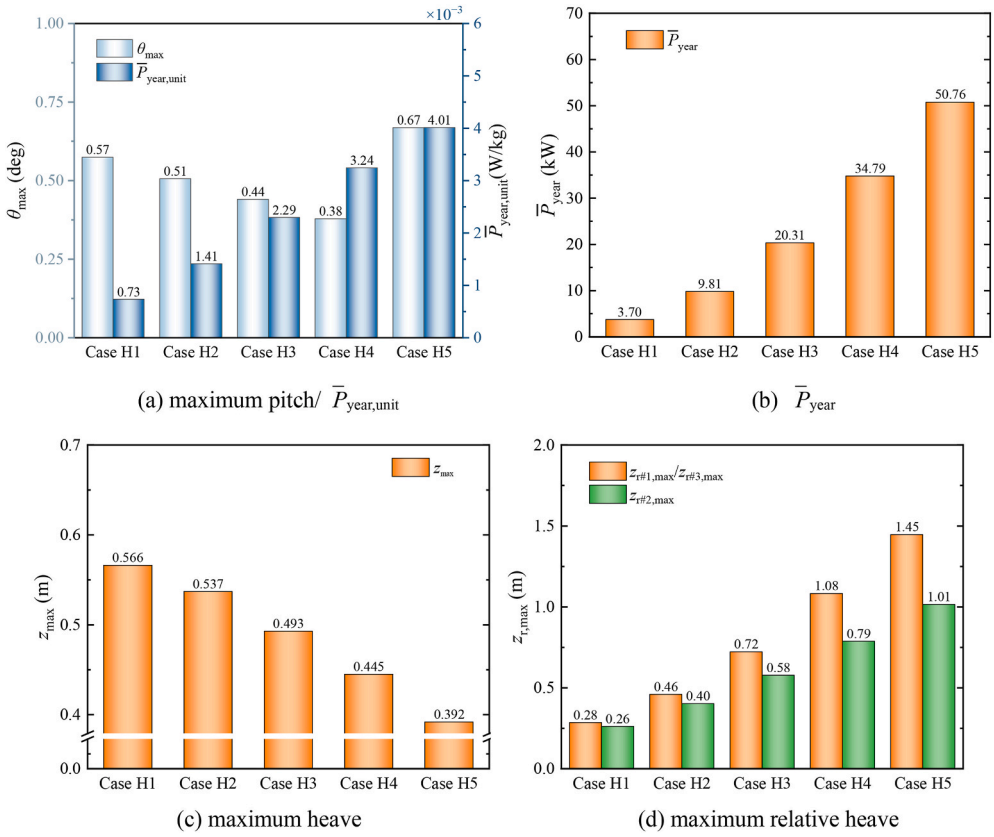

Fig. 21. Hybrid system maximum motion and $\overline{P}_{\text{year, unit}}$ at different masses.

Based on the preceding analysis of PTO parameter effects and the optimization results of various cases, it can be observed that the integration of built-in WECs plays a crucial role in pitch motion reduction of the platform during the multi-objective optimization process. The underlying principle is that the PTO system introduces a new coupled resonant peak into the platform's original pitch response curve and alters the shape of the original peak. By appropriately configuring the PTO parameters, the pitch response amplitude of the platform at periods corresponding to large wave heights can be effectively reduced, thereby reducing the maximum pitch motion that could occur under the operational sea conditions.

However, during the optimization process, a slight increase in pitch responses is generally observed in the short-period range (near the PTO pitch resonant period). This local motion response amplification, however, is effectively controlled in the global optimization and does not lead to extreme pitch motions as seen in the Case A series, indicating that such global optimization ensures the motion safety of the system. It is worth noting that in Case G, some cases with relatively high PTO damping achieve a certain degree of pitch reduction even within the short-period resonant range. This phenomenon provides valuable data support for future optimization strategies based on period segmentation or dynamic optimization combined with real-time wave monitoring.

6. Conclusions

The study focuses on a hybrid system composed of a 10 MW floating wind turbine and three built-in WECs. Using a frequency-domain wave-structure interaction calculation method combined with the NSGA-II multi-objective optimization algorithm, a global optimization strategy for simultaneously reducing platform motions and enhancing wave energy power generation is identified and systematically analyzed. In addition, the effects of the three key PTO parameters on the system are investigated, revealing their influence on the Pareto front trade-off and the pitch motion reduction mechanism of the built-in WECs. The main conclusions are summarized as follows.

(1) A comparative analysis of the hybrid system's motion response and power generation performance under different optimization strategies is conducted. The results indicate that the optimization strategy for a single sea state with high occurrence probability may lead to abnormally large pitch responses in adjacent period ranges, with wave energy absorption concentrated within a narrow frequency band. In contrast, global optimizing based on a range of operational sea states effectively avoids these issues. Moreover, the results indicate that the selection of operational sea states has a limited impact on the final optimization results and does not alter the overall optimization trend.

(2) The multi-objective optimization targeting the maximum pitch response and the annual average power generation per unit mass ($\overline{P}_{\text{year, unit}}$) significantly improves the system's economic efficiency and energy use. Compared with the optimization based on the annual average power generation, the optimization based on $\overline{P}_{\text{year, unit}}$ achieves a higher power generation performance per unit mass while maintaining a nearly constant pitch attenuation. The results indicate that the platform's maximum pitch motion is reduced by up to 48 % compared with the single platform.

(3) The stiffness and mass of the PTO system in the built-in WECs influence the resonant peak values and periods in the platform's pitch and heave directions, while also influencing the peak power generation of the WECs and the corresponding periods. Notably, an increase in mass and a decrease in stiffness produce similar trends in terms of both system power generation and motion performance. Changes in PTO damping have a moderating effect on the resonant peak values in pitch and heave, but their influence on the resonant period is relatively limited. However,

damping significantly affects the bandwidth of the WECs' energy absorption.

(4) To enhance power generation, the PTO resonant period in the pitch mode should be designed to avoid the high wave-height periods and shift toward shorter-period regions. Based on the evolutionary trend of multiple optimal solutions, the PTO resonant period generally increases as the system transitions from a "motion-reduction-prioritized" to a "power-generation-prioritized" optimization. These changes in resonant periods depend on the adjustment of the ratio of mass to stiffness and require appropriate damping to achieve optimal power generation performance.

(5) The key mechanism by which the hybrid system achieves motion reduction is the introduction of a new coupled resonant peak through the PTO system, which alters the shape of the platform's original pitch response peak. Proper configuration of the PTO parameters can significantly reduce the platform's pitch response in the period range corresponding to high wave heights, thereby effectively reducing the maximum pitch motion that may occur under operational sea states and enhancing the operational stability of the system.

In the present study, wind turbine aerodynamic loading and the dynamic contributions of the tower and upper structures are not explicitly included in the analysis. This simplification is mainly associated with the frequency-domain-based optimization framework adopted in this work, in which fully coupled aero-hydro dynamic interactions cannot be directly represented. Wind loads mainly contribute to a steady mean component, primarily affecting the equilibrium position of the platform (Zhou et al., 2023c) (Zhou et al., 2023d), while having a limited influence on the dynamic response amplitude that is of primary interest in this study. Therefore, the present results mainly reflect wave-driven system behavior under the present controlled modeling conditions. Future work will focus on developing a frequency-time domain optimization transition framework to enable more comprehensive optimization considering fully coupled aero-hydro dynamic effects.

CRediT authorship contribution statement

Yi Xiao: Writing – review & editing, Writing – original draft, Visualization, Validation, Software, Resources, Methodology, Investigation, Formal analysis, Data curation, Conceptualization. **Zedong Wang:** Visualization, Validation, Methodology, Investigation, Conceptualization. **Peng Jin:** Supervision, Software, Methodology, Funding acquisition. **Hongkun Zhuang:** Visualization, Resources, Investigation. **Wenhua Zhao:** Writing – review & editing, Formal analysis, Data curation. **Jian Tan:** Writing – review & editing, Methodology, Data curation. **Binzhen Zhou:** Supervision, Software, Resources, Project administration, Funding acquisition, Formal analysis, Data curation, Conceptualization.

Declaration of competing interest

The authors declare that they have no known competing financial interests or personal relationships that could have appeared to influence the work reported in this paper.

Acknowledgements

The author gratefully acknowledges Professor Guoxiong Wu (University College London) for his valuable guidance and insightful corrections on the methodology. The work is supported by the National Natural Science Foundation of China (52571291), Fundamental Research Funds for the Central Universities (2025ZYGXZR026, 2024ZYGXZR042), Guangdong Basic and Applied Basic Research Foundation (2024A1515240006), Project of State Key Laboratory of Subtropical Building and Urban Science (2023ZB14), and Stable Support Scientific Research Open Fund of China Ship Scientific Research Center (WDZC70202010207).

References

Abbasi, K., Shahbaz, M., Zhang, J., et al., 2022. Analyze the environmental sustainability factors of China: the role of fossil fuel energy and renewable energy. Renew. Energy 187, 390–402.

Allen, C., Viscelli, A., Dagher, H., et al., 2020. Definition of the Umaine VolturnUS-S Reference Platform Developed for the IEA Wind 15-megawatt Offshore Reference Wind Turbine. National Renewable Energy Lab.(NREL), Golden, CO (United States); Univ. of Maine, Orono, ME (United States).

Beirão, P., Mendes, M., 2025. Advances in offshore wind and wave Energies—2nd edition. J. Mar. Sci. Eng. 14 (1), 25.

Chen, Z., Zhou, B., Zhang, L., et al., 2018. Experimental and numerical study on a novel dual-resonance wave energy converter with a built-in power take-off system. Energy 165, 1008–1020.

da Silva, L., Sergiienko, N., Cazzolato, B., et al., 2022. Dynamics of hybrid offshore renewable energy platforms: heaving point absorbers connected to a semi-submersible floating offshore wind turbine. Renew. Energy 199, 1424–1439.

Deb, K., Pratap, A., Agarwal, S., et al., 2002. A fast and elitist multiobjective genetic algorithm: NSGA-II. IEEE Trans. Evol. Comput. 6 (2), 182–197.

Det Norske Veritas (DNV), 2010. Environmental Conditions and Environmental Loads. Recommended practice: DNV-RP-C205.

Det Norske Veritas (DNV), 2011. Modelling and Analysis of Marine Operations. Recommended Practice: DNV-RP-H103.

Deutch, J., 2020. Is net zero carbon 2050 possible? Joule 4 (11), 2237–2240.

Duarte, T., Price, S., Peiffer, A., et al., 2022. Windfloat Atlantic Project: Technology Development Towards Commercial Wind farms//Offshore Technology Conference. OTC. D021S016R003.

Farghali, M., Osman, A., Mohamed, I., et al., 2023. Strategies to save energy in the context of the energy crisis: a review. Environ. Chem. Lett. 21 (4), 2003–2039.

Ferrari, F., Besio, G., Cassola, F., et al., 2020. Optimized wind and wave energy resource assessment and offshore exploitability in the Mediterranean Sea. Energy 190, 116447.

Gunantara, N., 2018. A review of multi-objective optimization: methods and its applications. Cogent Eng. 5 (1), 1502242.

Hu, J., Zhou, B., Vogel, C., et al., 2020. Optimal design and performance analysis of a hybrid system combing a floating wind platform and wave energy converters. Applied energy 269, 114998.

Huang, S., Wang, J., Yang, M., et al., 2024. Parameter analysis and dual-objective optimization of the hydraulic power take-off system of a floating wind-wave hybrid system. Ocean Eng. 307, 118058.

Huang, X., Zheng, Z., Jin, P., et al., 2025a. Numerical optimization and experimental study on the hybrid system of pendulum wave energy converter and floating breakwater. Energy, 136914.

Huang, S., Liu, H., Liu, W., et al., 2025b. Optimal design and performance analysis of a combined wind-wave energy utilization device under wave environment near islands and reefs. Phys. Fluids 37 (2).

Huang, X., Ye, B., Wang, T., et al., 2025c. Multi-objective optimization of oscillating water column wave energy converter. Phys. Fluids 37 (7).

Jansen, M., Staffell, I., Kitzing, L., et al., 2020. Offshore wind competitiveness in mature markets without subsidy. Nat. Energy 5 (8), 614–622.

Jin, P., Zheng, Z., Zhou, Z., et al., 2023a. Optimization and evaluation of a semi-submersible wind turbine and oscillating body wave energy converters hybrid system. Energy 282, 128889.

Jin, P., Zheng, Z., Zhou, Z., et al., 2023b. Optimization and evaluation of a semi-submersible wind turbine and oscillating body wave energy converters hybrid system. Energy 282, 128889.

Johnston, B., Foley, A., Doran, J., et al., 2020. Levelised cost of energy, A challenge for offshore wind. Renew. Energy 160, 876–885.

Lambora, A., Gupta, K., Chopra, K., 2019. Genetic algorithm-A Literature review//2019 International Conference on Machine Learning, Big Data, Cloud and Parallel Computing (Comitcon). IEEE, pp. 380–384.

Li, Y., Yan, S., Shi, H., et al., 2023. Hydrodynamic analysis of a novel multi-buoy wind-wave energy system. Renew. Energy 219, 119477.

Lin, C., Zhang, Q., Sheng, S., et al., 2025. Novel design and performance evaluation of a hybrid system of floating offshore wind turbine and sharp-eagle WECs. Ocean Eng. 340, 122387.

Masciola, M., Jonkman, J., Robertson, A., 2014. Extending the capabilities of the mooring analysis program: a survey of dynamic mooring line theories for integration into FAST. In: International Conference on Offshore Mechanics and Arctic Engineering, vol. 45530. American Society of Mechanical Engineers. V09AT09A032.

McKay, M., Beckman, R., Conover, W., 1979. Comparison of three methods for selecting values of input variables in the analysis of output from a computer code. Technometrics 21 (2), 239–245.

Michailides, C., Luan, C., Gao, Z., et al., 2014. Effect of Flap Type Wave Energy Converters on the Response of a Semi-submersible Wind Turbine in Operational conditions//International Conference on Offshore Mechanics and Arctic Engineering, vol. 45547. American Society of Mechanical Engineers. V09BT09A014.

Muliawan, M.J., Karimirad, M., Moan, T., 2013. Dynamic response and power performance of a combined spar-type floating wind turbine and coaxial floating wave energy converter. Renew. Energy 50, 47–57.

Mwasilu, F., Jung, J., 2019. Potential for power generation from ocean wave renewable energy source: a comprehensive review on state-of-the-art technology and future prospects. IET Renew. Power Gener. 13 (3), 363–375.
Neshat, M., Sergiienko, N., Nezhad, M., et al., 2024. Enhancing the performance of hybrid wave-wind energy systems through a fast and adaptive chaotic multi-objective swarm optimization method. Appl. Energy 362, 122955.
Rehman, S., Alhems, L.M., Alam, M.M., et al., 2023. A review of energy extraction from wind and ocean: technologies, merits, efficiencies, and cost. Ocean Eng. 267, 113192.
Robertson, A., 2014. Definition of the Semisubmersible Floating System for Phase II of OC4. NREL Technical Report, NREL/TP-5000-60601.
Roddier, D., Cermelli, C., Aubault, A., et al., 2010. WindFloat: a floating foundation for offshore wind turbines. J. Renew. Sustain. Energy 2 (3), 033104.
Ruehl, K., Michelen, C., et al., 2014. Preliminary verification and validation of WEC-Sim, an open-source wave energy converter design tool. In: Proceedings of the 33rd International Conference on Ocean, Offshore and Arctic Engineering. OMAE, San Francisco, CA, 2014.
Soares-Ramos, E., de Oliveira-Assis, L., Sarrias-Mena, R., et al., 2020. Current status and future trends of offshore wind power in Europe. Energy 202, 117787.
Taveira-Pinto, F., Rosa-Santos, P., Fazeres-Ferradosa, T., 2020. Marine renewable energy. Renew. Energy 150, 1160–1164.
Teng, B., Taylor, R., 1995. New higher-order boundary element methods for wave diffraction/radiation. Appl. Ocean Res. 17 (2), 71–77.
Wang, J., Azam, W., 2024. Natural resource scarcity, fossil fuel energy consumption, and total greenhouse gas emissions in top emitting countries. Geosci. Front. 15 (2), 101757.
Wang, Z., Hu, J., Wang, Y., et al., 2025a. Nonlinear dynamic response of long flexible wind turbine blades based on intrinsic geometrically exact theory. Energy, 138791.
Wang, Z., Hu, J., Wang, Y., et al., 2025b. Nonlinear aeroelastic performance in 5MW and 15MW wind turbine blades using intrinsic geometrically exact method. Renew. Energy, 124581.
Xiao, Y., Ye, B., Zhang, H., et al., 2025. Optimization of motion and power performance of a wind-wave hybrid system with built-in wave energy converters. Energy 339, 139110.
Yin, D., Indergård, R., Lie, H., et al., 2024. Experimental investigation of towing of a semi-submersible floating offshore wind turbine. J. Phys.: Conference Series. IOP Publishing 2875 (1), 012026.
Yu, W., Müller, K., Lemmer, F., 2018. Qualification of Innovative Floating Substructures for 10 MW Wind Turbines and Water Depths Greater than 50 M. University of Stuttgart.
Zahle, F., Barlas, T., Lonbaek, K., et al., 2024. Definition of the IEA Wind 22-Megawatt Offshore Reference Wind Turbine. National Renewable Energy Laboratory (NREL), Golden, CO (United States).
Zhang, H., Wang, H., Zhou, X., et al., 2025. Numerical investigation of a three-dimensional integrated system combining an inertial built-in wave energy converter array and a floating breakwater. Energy 326, 136102.
Zheng, Z., Hu, J., Huang, Q., et al., 2025. Optimization of dual-module floating photovoltaic arrays: layout configuration and damping mechanisms for enhanced stability and energy performance. Energy, 136879.
Zhou, B., Hu, J., Zhang, Q., et al., 2023a. Optimal design and performance analysis of a hybrid system combining a semi-submersible wind platform and point absorbers. J. Mar. Sci. Eng. 11 (6), 1190.
Zhou, B., Hu, J., Jin, P., et al., 2023b. Power performance and motion response of a floating wind platform and multiple heaving wave energy converters hybrid system. Energy 265, 126314.
Zhou, B., Zheng, Z., Hu, J., et al., 2023c. Annual performance and dynamic characteristics of a hybrid wind-wave floating energy system at a localized site in the north sea. Ocean Eng. 280, 114872.
Zhou, B., Hu, J., Wang, Y., et al., 2023d. Coupled dynamic and power generation characteristics of a hybrid system consisting of a semi-submersible wind turbine and an array of heaving wave energy converters. Renew. Energy 214, 23–38.
Zhou, B., Xiao, Y., Ding, K., et al., 2024. Optimal strategy of the asymmetric wave energy converter survival in extreme waves. Phys. Fluids 36 (5).
Zhu, K., Cao, F., Wang, T., et al., 2024. A comparative investigation into the dynamic performance of multiple wind-wave hybrid systems utilizing a full-process analytical model. Appl. Energy 360, 122761.